Deep–Sea Research I 176 (2021) 103606

Contents lists available at ScienceDirect

Deep-Sea Research Part I

journal homepage: www.elsevier.com/locate/dsri

Bottom current control on sediment deposition between the Iselin Bank and the Hillary Canyon (Antarctica) since the late Miocene: An integrated seismic-oceanographic approach

R. Conte [a,b], M. Rebesco [a,*], L. De Santis [a], F. Colleoni [a], M. Bensi [a], A. Bergamasco [c], V. Kovacevic [a], J. Gales [d], F. Zgur [a], D. Accettella [a], L. De Steur [e], L. Ursella [a], R. McKay [f], S. Kim [g], R.G. Lucchi [a,h], the IODP Expedition 374 Scientists

[a] National Institute of Oceanography and Applied Geophysics – OGS, Trieste, Italy
[b] Department of Environmental Sciences, Informatics and Statistics, Ca' Foscari University of Venice, Venice, Italy
[c] Marine Science Institute of the National Research Council, ISMAR-CNR, Venezia, Italy
[d] School of Biological and Marine Sciences, University of Plymouth, Plymouth, UK
[e] Norwegian Polar Institute, Tromsø, Norway
[f] Antarctic Research Centre, Victoria University of Wellington, Wellington, New Zealand
[g] Korea Polar Research Institute, Incheon, South Korea
[h] Centre for Arctic Gas Hydrate, Environment and Climate (CAGE), UiT, The Arctic University of Norway, Tromsø, Norway

ARTICLE INFO

Keywords:
Contourite drift
Seismics
Oceanography
Ross Sea Bottom Water
Antarctic Slope Current
International Ocean Discovery Program
Expedition 374

ABSTRACT

In this paper we analyze how oceanic circulation affects sediment deposition along a sector of the Ross Sea continental margin, between the Iselin Bank and the Hillary Canyon, and how these processes evolved since the Late Miocene. The Hillary Canyon is one of the few places around the Antarctic continental margin where the dense waters produced onto the continental shelf, mainly through brine rejection related to sea ice production, flow down the continental slope and reach the deep oceanic bottom layer. At the same time the Hillary Canyon represents a pathway for relatively warm waters, normally flowing along the continental slope within the Antarctic Slope Current, to reach the continental shelf. The intrusion of warm waters onto the continental shelf produces basal melting of the ice shelves, reduces their buttressing effect and triggers instabilities of the ice sheet that represent one of the main uncertainties in future sea level projections. For this study we use seismic, morpho-bathymetric and oceanographic data acquired in 2017 by the R/V OGS Explora. Seismic profiles and multibeam bathymetry are interpreted together with age models from two drilling sites (U1523 and U1524) of the International Ocean Discovery Program (IODP) Expedition 374. Oceanographic data, together with a regional oceanographic model, are used to support our reconstruction by showing the present-day oceanographic influence on sediment deposition. Regional correlation of the main seismic unconformities allows us to identify eight seismic sequences. Seismic profiles and multibeam bathymetry show a strong influence of bottom current activity on sediment deposition since the Early Miocene and a reduction in their intensity during the mid-Pliocene Warm Period. Oceanographic data and modelling provide evidence that the bottom currents are related to the dense waters produced on the Ross Sea continental shelf and flowing out through the Hillary Canyon. The presence of extensive mass transport deposits and detachment scarps indicate that also mass wasting participates in sediment transport. Through this integrated approach we regard the area between the Iselin Bank and the Hillary Canyon as a Contourite Depositional System (ODYSSEA CDS) that offers a record of oceanographic and sedimentary conditions in a unique setting. The hypotheses presented in this work are intended to serve as a framework for future reconstructions based on detailed integration of lithological, paleontological, geochemical and petrophysical data.

* Corresponding author.
E-mail address: mrebesco@inogs.it (M. Rebesco).

https://doi.org/10.1016/j.dsr.2021.103606
Received 16 September 2020; Received in revised form 12 July 2021; Accepted 24 July 2021
Available online 5 August 2021

1. Introduction

One of the main uncertainties in future sea level projections is how the ice sheets will respond to global warming, in particular how much of Antarctica is losing ice mass through its large ice shelves. Warm oceanic waters and relative heat flow towards the ice shelf, causing basal melting of the Antarctic ice shelves, could reduce their buttressing effect and trigger instabilities (Joughin and Alley, 2011; Wåhlin et al., 2020). Similarly in the Arctic, the transport of heat by sea currents generates the progressive melting of sea ice and glaciers, which in turn substantially impact local circulation (Davison et al., 2020). Consequently, the study on how the ice sheets and the oceans interacted in the past provides important constraints to improve numerical ice sheet models and sea level projections.

Bathymetric troughs on the continental shelf and deep incisions across the continental slope represent preferential pathways for the exchange between dense shelf waters flowing down the continental slope and warm waters flowing upslope towards the continental shelf and the ice shelf base (Morrison et al., 2020). The Hillary Canyon, along the Ross Sea continental slope, forms a conduit for one of the largest outflows of dense waters in the Ross Sea, but is also located beneath an area of focused penetration of warm waters via the Pennell and Glomar-Challenger Basins (Orsi and Wiederwohl, 2009; Dinniman et al., 2011; Tinto et al., 2019; Morrison et al., 2020). Consequently, it is an optimal spot to reconstruct how oceanic circulation has regulated past heat flux onto the Antarctic continental shelf and past ice sheet advances/retreats.

The study area is located on the eastern edge of the Iselin Bank and on the continental rise west to the Hillary Canyon, at about 74° S (Fig. 1). Thick sedimentary deposits are preserved here and form the focus of this study. These have been previously interpreted as the product of the combined action of turbiditic and westward-flowing bottom currents resulting in a mixed turbiditic and contouritic depositional system, as it is the case in other sectors of the Antarctic continental margin (Escutia et al., 2002; Rebesco et al., 2002; Donda et al., 2007; Uenzelmann-Neben and Gohl, 2014; Hernández-Molina et al., 2017; Kim et al., 2018; McKay et al., 2019). These depositional systems, in some cases also including Mass Transport Deposits (Laberg and Camerlenghi, 2008), make up the continental rise and offer an indirect, but more continuous record of the combined glacial and oceanic depositional activity (Barker and Camerlenghi, 2002; Grützner et al., 2003). However in the Ross Sea sector, the continental rise is less explored than the continental shelf, where numerous geophysical and geological data have been collected in order to reconstruct the ice sheet advances/retreats directly where it was grounding (Hayes and Frakes, 1975; Anderson and Bartek, 1992; Bart, 2003; Bart and De Santis, 2012; McKay et al., 2016).

To explore the dominant glacial and oceanic processes acting in the area between the Iselin Bank and the Hillary Canyon, new seismic, morpho-bathymetric and oceanographic data were collected during the 2017 Antarctic expedition of R/V OGS Explora (Fig. 2). In 2018, the International Ocean Discovery Program (IODP) Expedition 374 drilled a total of five sites as part of an outer continental shelf to rise transect to investigate past ocean-ice sheet interactions (McKay et al., 2019) and two of these sites (U1523 on the southeastern flank of the Iselin Bank and U1524 on the eastern levee of the Hillary Canyon) are located within the focus area of this study.

Here, we present an integrated seismostratigraphic and oceanographic analysis obtained by combining experimental data collected in 2017 with the initial age models from IODP Expedition 374 (McKay et al., 2019). We also integrate these data with oceanographic modelling to inform how present-day ocean circulation influences sedimentary processes in these regions and how these processes have evolved in the Ross Sea sector since the Early Miocene.

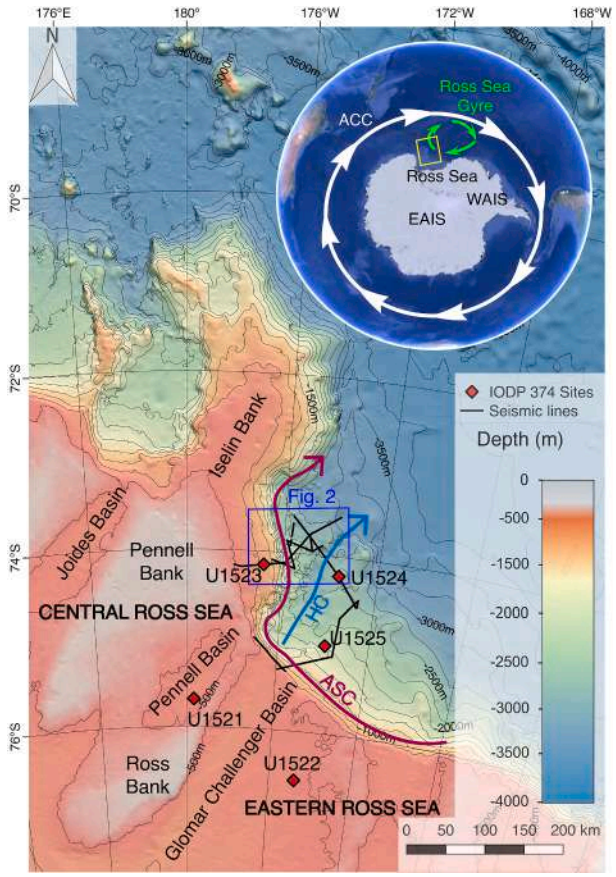

Fig. 1. IBCSO bathymetry (Arndt et al., 2013) including the study area with location of newly acquired seismic lines (ANTSSS and ODYSSEA projects) and International Ocean Discovery Program (IODP) Expedition 374 drilling sites (red diamonds). Isobaths every 500 m. The arrows are showing the approximate directions of Hillary Canyon (HC) (blue arrow) and of the core of the Antarctic Slope Current (ASC, purple arrow). Location of Fig. 2 is shown (blue rectangle). In the inset: Antarctic ice sheet with Antarctic Circumpolar Current (ACC), Ross Sea Gyre, West Antarctic Ice Sheet (WAIS), East Antarctic Ice Sheet (EAIS) and the study area (yellow rectangle).

1.1. Geological setting

The Ross Sea opened as a result of the separation of the blocks forming West Antarctica from the East Antarctic Craton during Late Mesozoic and Cenozoic (Cande et al., 2000; Luyendyk et al., 2001; Eagles et al., 2004; Decesari et al., 2007; Davey et al., 2016; Granot and Dyment, 2018). This separation led to crustal thinning that caused the formation of North-South trending rift grabens (Cooper and Davey, 1985; LeMasurier, 1990; Behrendt et al., 1991; Luyendyk et al., 2001; Wilson and Luyendyk, 2009). The Pennell and Ross Banks, propagating from the front of the Ross Ice Shelf to the Iselin Bank (Salvini et al., 1997), where the study area is located (Fig. 1), embody one of these North-South trending structural highs.

The Pennell Bank and the Ross Bank are bounded to the east by the Pennell Basin and the Glomar Challenger Basin respectively, that join at the shelf break in correspondence with the head of the Hillary Canyon (Fig. 1). The Hillary Canyon, at the eastern boundary of the investigated area, cuts the continental slope perpendicularly, in SSW-NNE direction. It is a pathway for glacial sediments (eroded and transported by ice streams from the innermost continental shelf to its edge) delivered to the deep sea as turbidity flows (Gales et al., 2021). These turbidity flows transport sediment down-slope, potentially contributing by overspilling of the suspended load to the construction of the levees of the Hillary Canyon. In the continental rise of the Ross Sea the gravity-driven

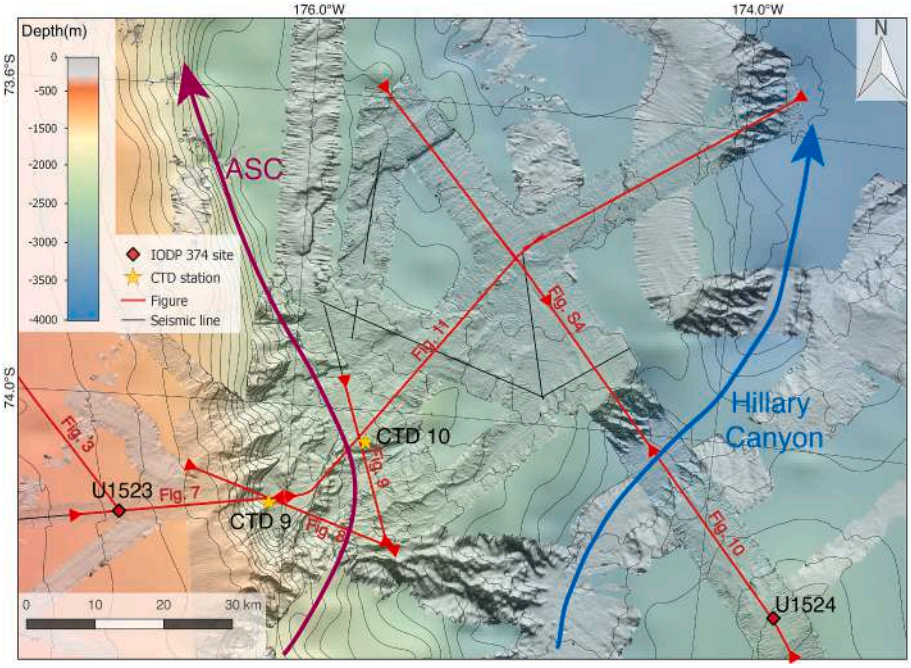

Fig. 2. The multibeam bathymetry superimposed on the GMRT (version 3.7; Ryan et al., 2009) and IBCSO bathymetry (Arndt et al., 2013). A clean version of this figure (withouth any interpretation and location of data) is shown in Fig. S1. Contour lines are plotted every 100 m. The navigation of seismic lines is plotted in black, with the position of the seismic transects shown in this paper highlighted in red. CTD stations 9 and 10 are plotted as yellow stars. International Ocean Discovery Program (IODP) Expedition 374 drilling sites are plotted as red diamonds. The purple arrow represents the direction of the Antarctic Slope Current (ASC) while the blue arrow highlights the Hillary Canyon downslope direction.

downslope flow of water and sediments act together with bottom currents and mass transports in building the sedimentary record at the base of the continental slope (Piper and Brisco, 1975; Lindeque et al., 2016; Kim et al., 2018).

On the continental shelf of the Ross Sea an average of 6 km of sediment thickness was deposited in three main Ross Sea basins (the Eastern, the Central and the Victoria Land basins) since the end of the early rifting phase. The Scientific Committee on Antarctic Research (SCAR) ANTarctic Offshore STRATigraphy (ANTOSTRAT) project (Cooper et al., 1995) compiled the Ross Sea Atlas map of the main, regional, seismic Ross Sea Sequences (from the oldest RSS-1 to the youngest RSS-8), constrained by drill core data from Deep Sea Drilling Project (DSDP) Leg 28 (Hayes and Frakes, 1975) and Cenozoic Investigations of the ROss Sea (CIROS) 1 project (Barrett, 1989) (Table 1). The age of the Ross Sea sequences was then better constrained in the western Ross Sea after the Cape Roberts and ANDRILL projects (Barrett et al., 1998, 2000; Naish et al., 2009). The oldest sequence, Ross Sea Sequence-1 (RSS-1), is filling the rift basins and is bound on top by the Ross Sea Unconformity (RSU) 6 inferred by DSDP Site 270 to be older than 26.7 Ma (McDougall, 1977; Kulhanek et al., 2019). Within RSS-1, Luyendyk et al. (2001) identified the unconformity RSU7, inferred to mark the end of the early rift phase and dividing this sequence into RSS-1 lower and RSS-1 upper. Sequences RSS-2 to RSS-5 were deposited during the Miocene and consist of glacially influenced sediments that gradually filled the shelf tectonic valleys (De Santis et al., 1995, 1999). The youngest sequences, RSS-6 to RSS-8, are believed to be of Late Miocene to Pleistocene age, when marine-based ice sheets are thought to have periodically expanded across much of the Ross Sea continental shelf during past glacial periods (Bart and De Santis, 2012). However, the correlation of seismic data with drill sites is ambiguous for RSS-6 to RSS-8 because they mostly have been eroded by the repeated ice sheet advances and retreats and due to difficulties in dating poorly consolidated, heavily reworked glacial sediments from the younger intervals in the DSDP Leg 28 cores (Hayes and Frakes, 1975). More recently the ANtarctic geological DRILLing (ANDRILL) AND-1B and AND-2A cores helped to shed new light on the Antarctic glacial history (Naish et al., 2009; McKay et al., 2012, 2016). During the Last Glacial Maximum (~21,000 years ago) the Antarctic Ice Sheet covered almost the entire Ross Sea continental shelf (Ship et al., 1999; Golledge et al., 2012; Anderson et al., 2014; Halberstadt et al., 2016; Bart and Cone, 2012; Prothro et al., 2018) and analogous expansions and retreats across the continental shelf are observed in drill cores and seismic data to have happened during earlier glacial phases (Naish et al., 2009; Bart and De Santis, 2012).

1.2. Oceanographic setting

The Antarctic Circumpolar Current (ACC) is the dominating circulation feature of the Southern Ocean. It flows clockwise around Antarctica and entrains North Atlantic Deep Water, a deep-water mass coming from the Atlantic Ocean, mixing it with other deep water masses coming from both Indian and Pacific Oceans (Orsi et al., 1999).

These mixed water masses form the Circumpolar Deep Water (CDW), identified by a ~1000 m thick layer of relatively salty, warm, and oxygen-deprived water that flows between the upper (colder and less salty) Antarctic Surface Water (AASW) and the lower (colder but with similar salinity) Antarctic Bottom Water (AABW, Sverdrup, 1940; Callahan, 1972; Orsi and Wiederwohl, 2009).

Some of the CDW is captured by the Ross Sea and Weddell Sea Gyres, large cyclonic circulation patterns to the south of ACC, which facilitate the southward transport of this water mass (Gouretski, 1999) onto the Antarctic continental margin.

In the Ross Sea, the gyre advects the CDW onto the continental shelf but this transport is partly prevented by potential vorticity constraints (Kohut et al., 2013) and by a hydrographic barrier due to a strong density front (the Antarctic Slope Front) located near the continental shelf break (Jacobs, 1991). This mechanism also occurs in other sectors of the Antarctic margin. The CDW mainly flows westward along the Ross Sea continental slope within the geostrophically adjusted Antarctic Slope Current (ASC) (Ainley and Jacobs, 1981; Whitworth et al., 1998) that sustains velocities of about 10–30 cm/s over the upper continental slope (Thompson et al., 2018), and its strength is modulated by the easterly winds. When the ASC encounters the Iselin Bank, in the Hillary Canyon area, its pathway is deviated northward (Fig. 1) but a smaller part enters onto the continental shelf through the head of the canyon.

Submarine canyons (e.g., the Hillary Canyon) and cross-shelf troughs (e.g., the Glomar-Challenger and Pennell basins) represent preferential pathways for a downslope flow of dense shelf water and upslope flow of

Table 1
Correspondence between unconformities interpreted in this work and the Ross Sea Unconformities (RSUs) originally defined by Brancolini et al. (1995), Cooper et al. (1991) and Hinz and Block (1984) within the ANTOSTRAT project. Preliminary age models from Integrated Ocean Discovery Program (IODP) Expedition 374 proceeding report (McKay et al., 2019) for sites U1523 and U1524 are shown in Fig. 4. The ages attributed at other sites of IODP Expedition 374, of DSDP leg 28 site 270, 271, 272, 273 (Chen, 1975; Ciesielski 1975; Hayes and Frakes, 1975; McDougall, 1977; D'Agostino and Webb, 1980; Leckie and Webb, 1986; Steinhauff and Webb, 1987; Savage and Ciesielski, 1983; Anderson and Bartek, 1992; Kulhanek et al., 2019) and that in Bart et al. (2011) are also shown.

Ross Sea Unconformity	IODP Exp. 374 (McKay et al., 2019)		DSDP Leg 28 (Brancolini et al., 1995; De Santis et al., 1995; Cooper et al., 1991; Anderson and Bartek, 1992)	IODP Exp. 374 Sites U1521 and U1522 (McKay et al., 2019)	Piston Core (Bart et al., 2011)
	Site U1523	Site U1524			
RSS-8					
RSU1			**0.7 Ma** at Site 271 (Chen, 1975) **0.65 Ma** at sites 270, 272, 273 (Hayes and Frakes, 1975; Savage and Ciesielski, 1983)		
RSS-7					
RSU2	2.5 Ma	2.5 Ma	**2.8-4 Ma** at Site 273 (Savage and Ciesielski, 1983) **<3 Ma** at Site 271 (Ciesielski, 1975)	**2 Ma** at Site U1522	**2 Ma** at NBP03-01A PC2
RSS-6					
RSU3	3-5 Ma	4.5 Ma	**Hiatus from 4 to 14.7 Ma** at Site 273 (Savage and Ciesielski, 1983) **10.5 Ma** (Brancolini et al., 1995)	**Hiatus from 5.5 to 8.5 Ma** at Site U1522	
RSS-5 upper					
RSU3a	11 Ma	9 Ma extrapolated			
RSS-5 lower					
RSU4	14.5 Ma extrapolated	NA	**14.1 Ma** at Site 272 (Hayes and Frakes, 1975) **Hiatus from 4 to 14.7 Ma** at Site 273 (Perez et al., 2021; Savage and Ciesielski, 1983)	**14.6-15.8 Ma** at Site U1521 (Perez et al., 2021)	
RSS-4					
RSU4a	NA	NA	**<19.2 Ma** at Site 272 (Savage and Ciesielski, 1983	**17 Ma** at Site U1521 (Perez et al., 2021)	
RSS-3					
RSU5	NA	NA	**<21.1 Ma** at Site 270 (Steinhauff and Webb, 1987)	**18 Ma** at Site U1521 (Perez et al., 2021)	
RSS-2					
RSU6	NA	NA	**>26.7 Ma** at Site 270 (D'Agostino and Webb, 1980; Leckie and Webb, 1986; Mcdougall, 1977; Kulhanek et al., 2019)		
RSS-1 upper					
RSU7	NA	NA	**Late Cretaceous** at Site 270 (Luyendyk et al., 2001)		
RSS-1 lower					

warmer CDW. Energetic downslope flows and cascading of dense water occur in few places of the Ross Sea (Budillon et al., 2011), which is one of the main sites of dense water formation around Antarctica (Jacobs et al., 1970). There, dense water produced mainly through brine rejection during sea ice formation, cooling and mixing with different shelf water masses, turns into Ross Sea Bottom Water (RSBW), which reaches the shelf break and cascades down the continental slope (Jacobs et al., 1985; Jacobs and Giulivi, 1999; Gordon, 2009). During their descent, dense water plumes mix with the CDW, modify their original properties and turn into AABW at larger depths. The cascading of dense waters through the Hillary Canyon has been described by Bergamasco et al. (2002) as a signal of very cold flow down the continental slope at the head of the canyon itself.

2. Data and methods

Oceanographic and geophysical data used in this study were acquired during the 2017 Antarctic expedition onboard the R/V OGS Explora, in the framework of the ANTSSS (ANTarctic ice Sheet Stability from continental Slope processes) Eurofleets2 EU project and the ODYSSEA (paleoclimatic reconstructions and Ocean DYnamics from the Sediment drifts of the ross SEA) Italian National Program for Antarctic Research (PNRA) project. Sediment core and well-log data used for time-depth conversion and age models were collected in 2018 during the IODP Expedition 374 (McKay et al., 2019).

2.1. Morpho-Bathymetric data acquisition and processing

About 2700 km^2 of multibeam bathymetry data were acquired, some of which together with seismic reflection profiles (Fig. 2). The hull-mounted multibeam echosounders used for this expedition are: a 12 kHz RESON SeaBat 7150 for the deeper areas, generating up to 880 beams with a beam width of 2° × 2°; a RESON SeaBat 8111 for the shallower parts, generating 101 beams with a beam width of 1,5° x 1,5°. Data were processed using the software PDS 2000, which allowed the generation of a 50 m × 50 m grid. The grid was imported in QGIS where we created a hillshade effect with a vertical exaggeration equal to 10 to evidence the structures. The new multibeam data were superimposed on the Global Multi-Resolution Topography (GMRT) synthesis (version 3.7; Ryan et al., 2009) at a grid resolution of 100m and on the International Bathymetric Chart of the Southern Ocean (IBCSO) bathymetry (Arndt et al., 2013) with a grid resolution of 500 m × 500 m in order to be able to observe also the general bathymetric features (Fig. 2).

2.2. Seismic data acquisition and processing

During the same expedition, about 700 km of high-resolution single-channel seismic reflection profiles were acquired (Table S1). The seismic source consisted of a linear array of two 210 cu.in. Generator Injector (GI) guns spaced 2 m apart. To produce a good quality signal while preventing severe energy loss, both the guns were shot in harmonic mode, with the injector and the generator working at the same volume of 105 cu.in. and at a pressure of 140 bar. The array was towed at a depth of 4 m, corresponding to a notch frequency around 180 Hz (that generally defines the upper limit of the amplitude spectrum) assuming a speed of sound in the water of 1450 m/s. The shot point interval was set at 8 s, which translates to a shot distance of 13–15 m at a nominal ship speed of 3.5–3.8 knots.

The receiver array consisted in a 9.5 m mini-streamer composed of 10 hydrophones, five of which spaced 0.625 m apart and the other five 1 m; the streamer was towed at a distance of around 35 m from the source and at a depth of around 1–1.5 m below the surface. Since the spacing between the hydrophones was very small with respect to the water depth, and the normal moveout correction negligible, the 10 traces were stacked for each shot during the processing resulting in a single-channel configuration. The recording time was set to 7 s at a sampling rate of 1 ms. According to the Rayleigh λ/4 criterion, the expected theoretical vertical resolution of the seismic data, assuming a central frequency of 130 Hz and sound speed of 1600 m/s, is of ca. 3 m. The high vertical resolution of newly acquired seismic profiles implies a lower penetration capacity (around 1–1.5 km) than previously collected multichannel seismic profiles in the area.

Seismic data were processed using the Vista software by Schlumberger. The processing procedure was as follows: 1- bandpass filtering, 2- deconvolution, 3- horizontal stacking and 4-amplitude gain. Finally, the sections were time-migrated using velocity models produced by the analysis of diffraction hyperbolas, given the impossibility of running velocity analysis on single-channel data.

2.3. Seismic data interpretation and time-depth conversion

The seismic data were interpreted using the IHS Kingdom software. The most significant unconformities were firstly identified solely within the crossing ODYSSEA and ANTSSS high-resolution seismic profiles. An attempt to correlate them between the continental shelf and the continental slope on both sides of the Hillary Canyon was made, but a direct correlation was not always possible due to erosion (of the uppermost sequences) and pinch-out (of the lowermost ones). To assist the correlation, all other relevant existing seismic profiles (publicly available through the Antarctic Seismic Data Library System: https://sdls.ogs.trieste.it) were used. Then the seismic sequences recognized in the new high-resolution dataset were matched with the regional RSSs and RSUs previously mapped in the ANTOSTRAT Atlas (Brancolini et al., 1995b) (Fig. 3). Thus the existing nomenclature was adopted (Cooper et al., 1987, 1991; Brancolini et al., 1995a; De Santis et al., 1999; Bart et al., 2000, 2003; Anderson et al., 2019), with the addition of a new unconformity (RSU3a, Table 1).

Seismic profiles were then correlated with well logs and stratigraphy of the IODP Expedition 374 sites U1523 and U1524 (McKay et al., 2019) (Fig. 1). Site U1523 was drilled to a depth of 307.8 m below seafloor (mbsf) and intercepted the unconformities from RSU2 to RSU4 (Fig. 3). However, the current age model (McKay et al., 2019) reaches a depth of only about 220 mbsf, according to the limits imposed by core recovery. Site U1524 was drilled to a depth of 441.9 mbsf and intercepted the unconformities from RSU2 to RSU3a, with the age constraints provided to the base of the hole.

The correlation of seismic profiles with age models of sites U1523 and U1524 provides constraints for the age ranges represented by the unconformities RSU3a to RSU2. A comparison with the ages attributed in previous works (Brancolini et al., 1995b; De Santis et al., 1999; Bart et al., 2011) and at other sites of the IODP Expedition 374 (McKay et al., 2019; Pérez et al., 2021a) was also made (Table 1). The age of the intercepted seismic unconformities at the two drill sites allowed also to check our correlation between the continental shelf and the continental

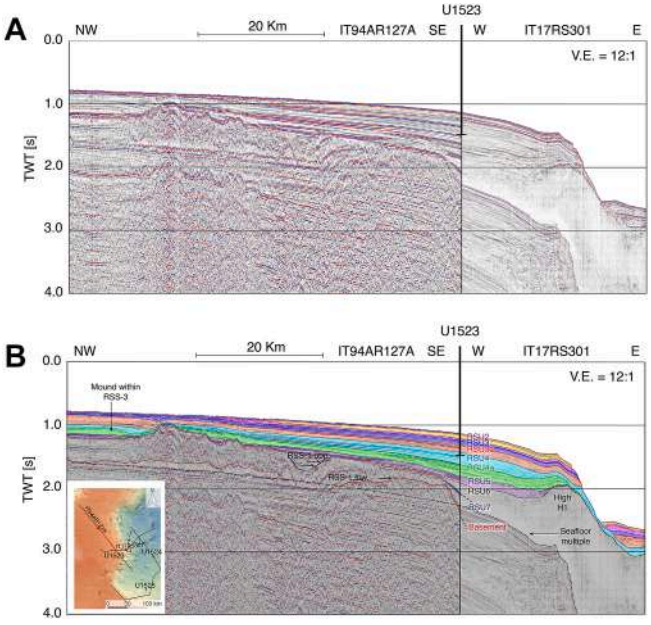

Fig. 3. Combination of seismic sections IT94AR127A (NW part) and IT17RS301 (eastern part) crossing at International Ocean Discovery Program (IODP) Site U1523 in seconds Two-Way travel Time (TWT). a) uninterpreted sections; b) interpreted sections. Seismic section IT17RS301 is shown with more details in Fig. 7. RSU7 and the basement cannot be identified in the line IT17RS301 (high resolution but low penetration). The location of the lines is shown in the inset.

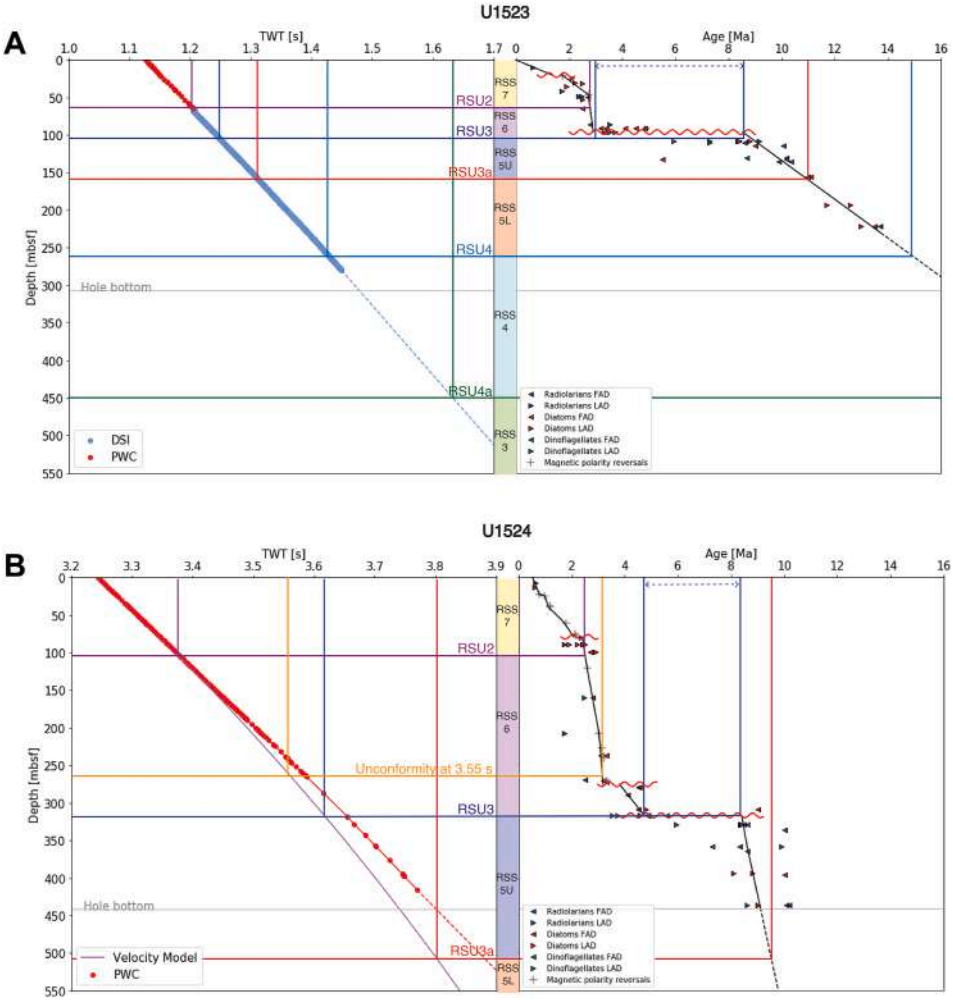

Fig. 4. Time-Depth chart and age models. a) site U1523: b) site U1524. The dashed parts in the Time-Depth chart indicate extrapolation by keeping constant the average velocity in correspondence of the last velocity value. At site U1524 the proposed time-depth conversion with a velocity linearly increasing from 1500 m/s at 0 mbsf to 2000 m/s at 400 mbsf (Velocity Model) is also plotted. In the age model the dashed parts are extrapolations by keeping constant the sedimentation rate in the lowermost part. Grey horizontal line indicates the maximum penetration reached at each site. The orange line represents an intermediate unconformity between RSU2 and RSU3. The age model (million years ago, Ma) and sediment analysis data related to U1523 and U1524 faunas are taken from IODP Expedition 374 Proceeding (McKay et al., 2019). TWT: two-way time in seconds (s); Depths are in meters below sea floor (mbsf); PWC: time-depth conversion obtained by using velocities measured with P-Wave Caliper; DSI: time-depth conversion obtained by using velocities measured with Dipole Sonic Imager tool string.

rise on both sides of the Hillary Canyon (Fig. 2).

To integrate the age models at the two sites with the seismic profiles, a Time-Depth chart that allows to convert the depth in mbsf to Two-Way travel Time (TWT) in seconds was produced (Fig. 4) by using seismic velocities measured after drilling. At Site U1523 the discrete measurements of seismic velocity, conducted on the working-half core sections using the P-wave caliper (PWC) in the upper 67 m (where wireline logging is not available), were combined with continuous, in situ measurements conducted downhole with the Dipole Sonic Imager (DSI) for the lower section down to 292 mbsf (McKay et al., 2019). At Site U1524 the PWC data were used down to the depth of 434 mbsf since the downhole logging tool was not run. However, the velocity measured at Site U1524 are uncertain as we detail in the discussion chapter. Thus, an alternative velocity model was considered for this Site, similar to that obtained with the tomographic inversion of travel times at ODP Site 1096 on Sediment Drift 7 of the Antarctic Peninsula margin (Volpi et al., 2001). For this scope, a seismic velocity linearly increasing from 1500 m/s at the seafloor to 2000 m/s at 400 mbsf was used, that results in a good match between a major hiatus in the cores with the adjacent major seismic unconformity (Fig. 4). To give an indicative thickness in meters of the described seismic features not crossed by the drilling sites a constant sound speed of 1600 m/s was used for the conversion in the results section.

2.4. Oceanographic data acquisition

The Sea-Bird Scientific 9 plus (SBE) probe, mounted on the SBE Carousel with 21 Niskin Bottles, was equipped with pressure, conductivity, and temperature sensors, as well as with WETLabs fluorescence and optical turbidity sensors. Two Conductivity-Temperature-Depth (CTD) profiles (stations 9 and 10) were acquired in February 2017 and approached the sea-bed within a distance of ~ 7–10 m (Fig. 2). Station 9 is located at the base of the continental slope at 74° 07.63′ S and 176° 04.91′ W and reaches 1800 m depth. Station 10 is located in the open ocean at 74° 02.50′ S and 175° 38.58’ W and reaches 2130 m depth (Fig. 5a–c). In this study, we use potential temperature (θ, °C), salinity (S), potential density (σ_θ, kg m^{-3}) and turbidity (expressed in Nephelometric Turbidity Unit - NTU) that were calculated from in situ data using the Seabird post-processing software. Data were quality checked and averaged every 1 dbar throughout the water column. Overall accuracies are within ± 0.002 °C for temperature, ± 0.005 for salinity.

A self-contained downward looking Lowered Acoustic-Doppler-Current-Profiler (LADCP, RDI Workhorse Sentinel model 300 kHz) mounted on the CTD-Rosette system was used to measure relative velocity profiles throughout the water column during the CTD casts (Fig. 5d). Vertical current profiles in 8 m bins were obtained by means of a software developed at Lamont-Doherty Earth Observatory at Columbia University (Version IX_10; Thurnherr, 2014, https://www.bodc.ac.uk/data/documents/nodb/pdf/ladcp_ldeo_processing_IX.7_IX.10.pdf). The associated velocity error depends on depth and varies from cast to cast. Median of the depth-dependent velocity error was 0.035 m/s at station 9, and 0.061 m/s at station 10 (Fig. 5d).

A vessel mounted ADCP (vmADCP, Ocean Surveyor model 75 kHz) acquired vertical profiles of the horizontal currents over three days in

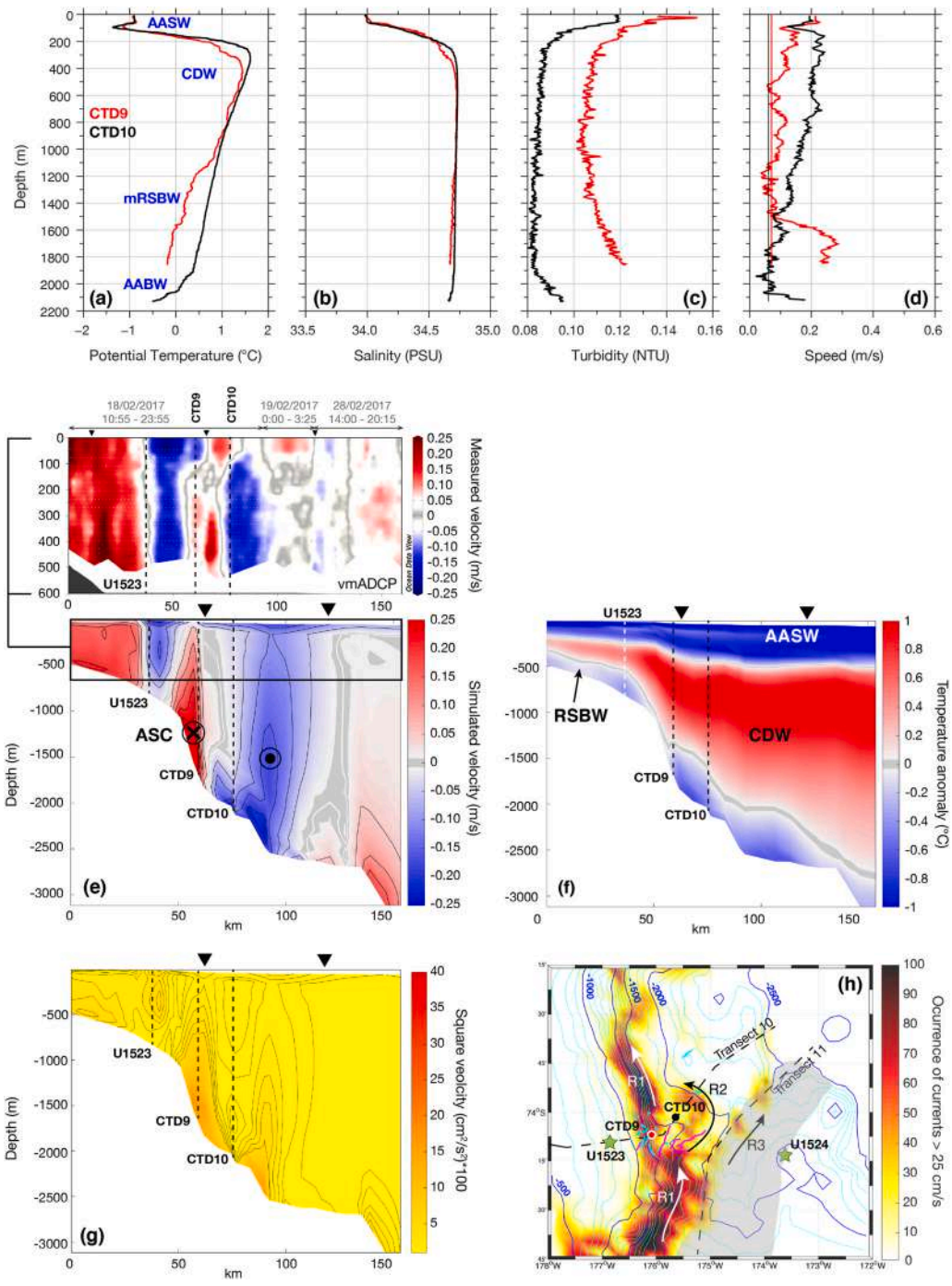

Fig. 5. Vertical profiles from CTD casts at two stations during the R/V OGS Explora campaign in 2017: potential temperature (a), salinity (b), turbidity (c), and current speed from the L-ADCP (d). Thin vertical lines in panel d indicate the predicted astronomical tidal speed near the two locations. CTD casts were carried out between 24 February (23.00 UTC) and 25 February (04.00 UTC). AASW: Antarctic Surface Water; CDW: Circumpolar Deep Water; mRSWB: modified Ross Sea Bottom Water. (e) Comparison between cross-track (v component) interpolated vmADCP horizontal velocity (m/s) measured in 2017 on February 18, 19 and 28 (top) along transect 10 (see panel h) and simulated horizontal velocities (m/s, bottom). Simulated velocities correspond to January 21, 2002 and are here only indicative and used for the sake of comparison (see animations in supplementary for model daily variability). (f) Simulated vertical temperature anomaly (relative to 0 °C isotherm) as of January 21, 2002. (g) Simulated square speed (U2 + V2, in cm^2/s^2) as of January 21, 2002. Square speed has been multiplied by 100 to improve the readability. (h) Simulated occurrence of bottom currents (%) with a cut-off imposed at 25 cm/s over a period of 5 years (1840 days) over the studied area. 100% indicate that strong currents always occur over the area. The interpreted sedimentary mounds' crest (magenta lines) and detachment scarps (cyan lines) are also shown. R1 to R3 correspond to the main pathways for cascading dense shelf waters described in the text. The Hillary Canyon is shown by a grey shaded area. Green stars indicate the location of the IODP 374 site 1523 and 1524. All simulated quantities and vmADCP have been interpolated along transect 10 (see panel h) and black triangles above each panel indicate the location where the transect changes orientation. The location of the two CTDs and of International Ocean Discovery Program (IODP) Sites U1523 and U1524 (green stars in 5h) are reported on all transects.

February 2017. After the suitable post-processing, using the CODAS package (https://currents.soest.hawaii.edu/docs/adcp_doc/codas_doc/index.html), horizontal current velocity components (u and v) were available in 16 m bins in the depth range between 44 and 500 m, at a time interval of 5 min. The vmADCP speed error was calculated, using the full depth speed profiles measured during each LADCP cast, as a median value of the absolute deviations from the time averaged profile. It amounted to 0.01 m/s at both stations, while maximum values were 0.05 and 0.07 m/s at station 9 and 10, respectively.

Due to the operational limitations, even when the seafloor depth fell within its measurement range, vmADCP was unable to provide measurements near the bottom, where the blind unmeasured portion usually corresponds to 10% of the water depth. The data gathered by the vmADCP covered depths up to 500–600 m and provided information regarding the spatial distribution of the flow present at the moment of the vessel's transit over the seismic lines. The flow in the upper part is temporally and spatially variable, both in speed and direction revealing an upper layer with strong mesoscale activity (Fig. 5e top). The measured meridional component of current speeds varied between −0.3 and 0.3 m/s, with larger values recorded in the area over the continental slope and in the proximity of the shelf break (Fig. 5e top). This timescale is by far shorter than the geological timescale at which the processes of interest in this study operate. However, the vmADCP data provides a necessary constraint to the numerical simulation (see below) in the upper layers.

Current velocities recorded with the LADCP and vmADCP were compared within the depth interval 40–100 m. The Root Mean Square (RMS) speed differences were between 0.05 and 0.06 m/s. This value is

similar to the speed uncertainty of the two measurement systems. However, the direction RMS differences were large and not constant, e.g., they were about 40° and 70° at stations 9 and 10, respectively. This prevents us from taking into account the direction measured by the LADCP. Hence, for the LADCP, we report only data on the current magnitude.

2.5. Regional oceanic circulation modelling

To understand the spatio-temporal variability of the main water masses flowing through the studied area, the ocean model Regional Ocean Modeling System (ROMS) as described in Mack et al. (2017) was chosen. It was used to estimate the seasonal to interannual evolution of Ross Sea oceanography from 2000 to 2014. The model domain is a cartesian 5-km horizontal resolution grid with 24 vertical sigma-layers, centered on the Ross Sea: from Victoria Land to Marie Byrd Land in the East-West direction and from slightly offshore the Iselin Bank up to the Ross Ice Shelf grounding line in the North-South direction. ROMS boundary conditions are the bathymetry from IBCSO (Arndt et al., 2013), ice shelf draft from BEDMAP2 (Fretwell et al., 2012), and atmospheric fluxes from Era-Interim datasets. Initial oceanic conditions were started from a previous ROMS 5-year spinup of the perpetual year 1998 reconstructed by the climatology of the Ross Sea from Dinniman et al. (2003).

In this study, we are mainly interested in the general behavior of water masses (i.e. mean horizontal velocities, pathway and strength, vertical temperature) that directly affect the geometry of the deposits on the multi-millennial timescale (Fig. 5 e-h). Since geological data do not reach seasonal or inter-decadal temporal resolution and the numerical simulation was started from an already validated and published state of the Ross Sea, we retain that the simulated oceanic conditions are representative of the main modern general circulation and water masses characteristics of the Ross Sea. A daily snapshot from January 21, 2002 was selected from the simulation for indicative comparison with vmADCP measurements and was used to support the geophysical analysis. Daily variability throughout austral summer 2002 is shown in Supplementary videos to further strengthen the discussion about the occurrence of the main local processes described here. Two transects were extracted from the simulation, Transect 10 (Fig. 5), that goes across the study area following the seismic profiles and Transect 11 (Fig. S2), that follows the western levee of the Hillary Canyon down to the study area (Fig. 5h for the locations). Full analysis of the outputs of the simulation is beyond the scope of this paper and will be the object of a dedicated manuscript.

3. Results

3.1. Multibeam bathymetry

The low resolution IBCSO bathymetry shows a concave shape of the continental shelf margin at about 75°S, that corresponds to the head of the Hillary Canyon (Fig. 1). The new multibeam bathymetry (Figs. 2 and 6), mainly covers the base of the continental slope and the continental rise of the eastern flank of the Iselin Bank, but some tracks are crossing the continental shelf and the Hillary Canyon. The multibeam swaths that cross perpendicular to the Hillary Canyon axis along the track of our seismic profile show that the canyon has a flat base, is about 7 km wide and has asymmetric levees (Fig. 6). The western levee is rougher and steeper (around 3°) than the eastern levee, with a slope of about 1.5°. The continental slope of the Iselin Bank, to the west of the Hillary Canyon, is generally oriented in a N–S direction, and it is slightly lobed (with westward inflections) between about 73°S and 72°S and between 73°S and 75°S (Fig. 1).

Among other mounds that we identified in our dataset, we outlined six mounds (M1-6 in Fig. 6) both on the continental shelf and rise (selected because they are completely imaged by multibeam and they

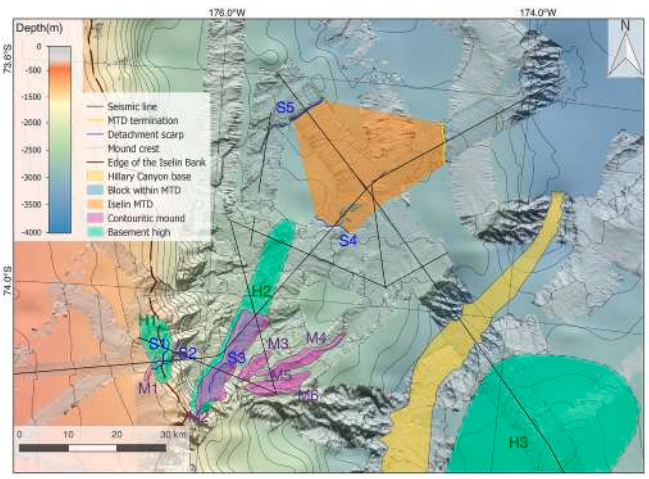

Fig. 6. Morpho-sedimentary interpretation superposed on the bathymetry of Fig. 2. The main morphologic features are highlighted: contouritic mounds M1 to M6 and their crests, detachment scars S1 to S5, Iselin Mass Transport Deposit and associated blocks and rise at its termination, the inferred extent of basement highs.

are crossed by the seismic data). They show an elongation subparallel (M1-2) or at low angle (M3-4) to the slope direction or almost perpendicular to the margin in correspondence of a change in the margin's trend (M5-6). Their heights span from tens to hundreds of meters, widths of few kilometers, and length from few to tens of kilometers (their geometrical characteristics are summarized in Table 2). The shaded relief superimposed on the IBCSO bathymetry highlights the occurrence of narrow and linear features in the upper part of the continental slope, as well as in the continental rise, that represent sub-vertical scarps. The scarps (Fig. 6, S1-5) have a relief ranging between 60 and 100 m. Scarp S1 (Fig. 6), which produces a vertical step of around 60 m in height, partially cuts mound M1 that lies on the eastern edge of the Iselin Bank. Just outward S1 we find the sub-vertical scarp S2, around 100 m high. These two scarps lie in a steep sector of the continental slope, reaching a dip of about 9°. As for M1, scarps often cut the mounds and produce steep flanks. An example is scarp S3, cutting the eastern flank of mound M2 with a sub-vertical surface about 100 m high. Scarps S4 and S5 lie in the continental rise, where the seafloor seaward dip is less than 1°. These two scarps are sub-vertical steps in the seafloor, of more than 100 m, that bound the western side of an internally chaotic body (Fig. 6, orange shade (in the web version), see section 3.2). The data coverage in this area is poor, therefore it is not possible to fully estimate the extent of this body. It is about 30 km long in SW-NE direction and 25 km long in NW-SE direction. The eastern termination of this feature, corresponds to a sea-bed rise about 15 m high and elongated in N–S direction (Fig. 6). Inside this body, some small features (ca. 1 km wide and about 25 m high) proximal to the scarp S4 show a topographic relief and a morphology rougher than the adjacent seafloor (blocks in blue (in the web version) in Fig. 6).

3.2. Seismostratigraphy

In the following, we describe the character of the seismic sequences, from the deepest to the shallowest. The ages attributed to each unconformity are summarized in Table 1 and discussed in section 4.1.

3.2.1. Description of seismic sequences

3.2.1.1. RSS-1. RSS-1, that is the deepest sequence, is better imaged in pre-existing seismic profiles that have lower resolution but higher penetration than the ones acquired in 2017 (Fig. 3). RSS-1 fills basement depressions and has sub-parallel internal reflections with poor lateral

Table 2
Summary of the geometrical characteristics of the mounds identified on the multibeam bathymetry. The elongation direction is intended as the angle with the continental slope direction (assumed to be perfectly N–S).

Mound Name	Elongation Direction (Ɛ)	Height (H)	Length (L)	Width (W)
M1	25°	5 m	5 Km	1 Km
M2	25°	200 m	20 Km	4 Km
M3	35°	20 m	8 Km	2 Km
M4	55°	30 m	20 Km	2 Km
M5	85°	20 m	2 Km	0.5 Km
M6	75°	70 m	15 Km	3 Km

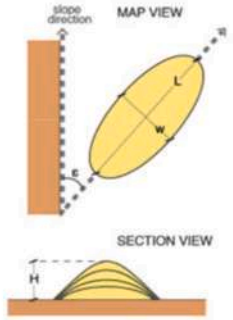

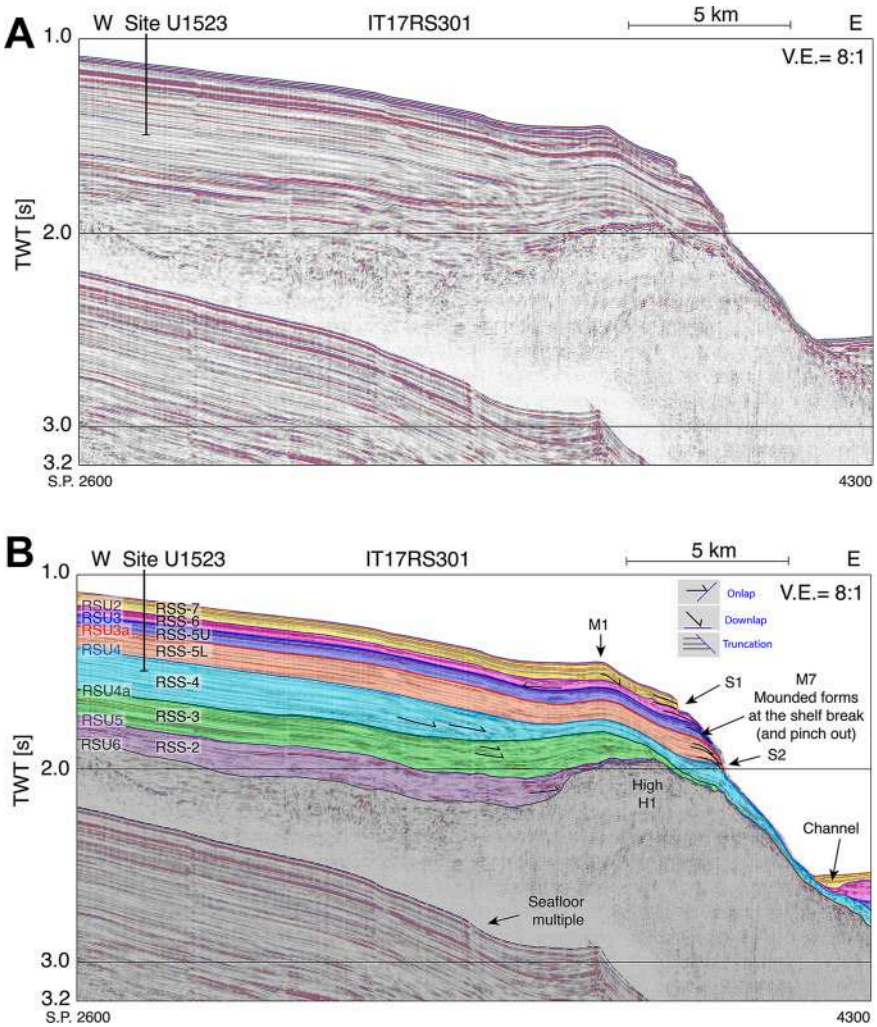

Fig. 7. Seismic section IT17RS301 in seconds Two-Way travel Time (TWT). a) uninterpreted section; b) interpreted section. Location of the International Ocean Discovery Program (IODP) Site U1523 is shown. The scarps are S1 and S2, M1 is the contouritic mound. M7 labels a contouritic deposit at the shelf break. Location of the section is shown in Fig. 2.

continuity. Over the Iselin Bank, RSS-1 is subdivided in RSS-1 lower and RSS-1 upper. RSS-1 lower is wedge-shaped, with reflections filling complex graben-like features. It is locally folded and tilted and is truncated by the sub-horizontal surface RSU7 (Fig. 3), a high-amplitude and continuous acoustic reflection. RSS-1 upper comprises subparallel and sub-horizontal reflections onlap terminated on the flanks of basement ridges. RSS-1 is bound on top by RSU6, a high amplitude and generally flat reflection that truncates at low angle the underlying strata. In 2017 seismic lines, RSU6 is the lowest reflection that can be mapped with confidence (Fig. 3). A high in RSU6 surface (H1) subparallel to the edge of the Iselin Bank bounds a depression filled by the overlying sequences (Figs. 7 and 8). Other highs in RSU6 occur close to the base of the continental slope (e.g H2 with SW-NE direction, Figs. 6 and 8) and, more pronounced, seawards (Fig. 9) and to the SE of the Hillary Canyon below Site U1524 (H3, Fig. 10, with more uncertain trend).

3.2.1.2. RSS-2. This sequence is characterized by generally sub-parallel reflections with low lateral continuity and medium to low amplitude that terminate in onlap on the ridges. The thickness of this sequence is strongly controlled by underlying morphology (Figs. 7 and 11) and it has the characteristics of a basin-filling deposit. RSS-2 at the top by RSU5 is characterized by a low angle surface.

3.2.1.3. RSS-3. Also this sequence has the characteristics of a basin-filling deposit but with reflections of higher amplitude and lateral continuity than those of RSS-2, closing in pinch out at the base of the continental slope (Figs. 8 and 11). On the inner part of the Iselin Bank, to the west of a high in RSU6, RSS-3 thickens in correspondence of upward convex internal reflections (Fig. 3). On top of H1, the reflections are laterally truncated by RSU4a at the top of RSS-3 (Figs. 8 and 9).

3.2.1.4. RSS-4. RSS-4 is made of sub-parallel low amplitude and occasionally high amplitude reflections. RSS-4 drapes over H1 and H2 (Figs. 7 and 9) and is the only sequence that can be traced across the continental slope, though the reflections are strongly deformed and lose lateral continuity (Figs. 7 and 8). This is the lowest sequence showing thickness variations to the east of H2 (Fig. 9) and close to the base of the continental slope (Figs. 8 and S3) that are not directly related to the underlying morphology. RSS-4 comprises mounds made by internal reflections with an upward convex shape. These mounds, similar in size

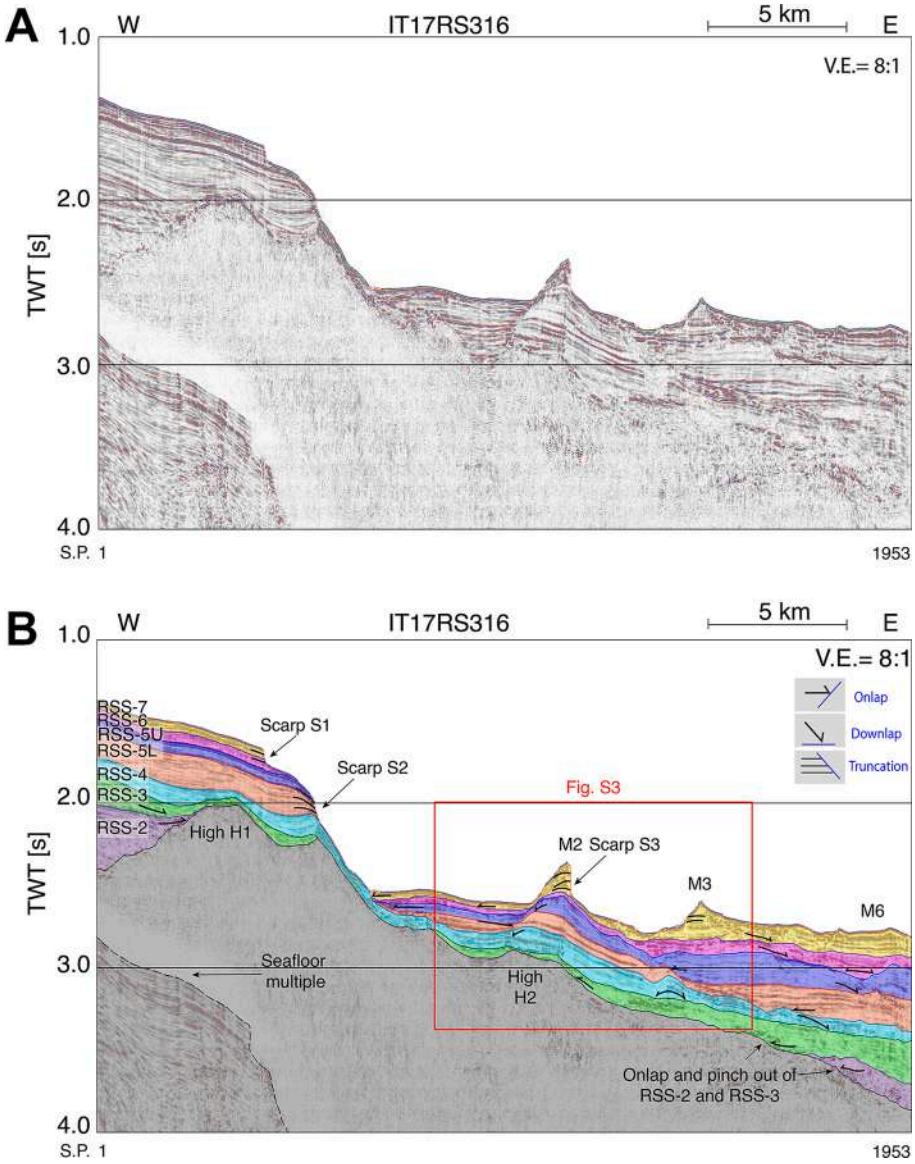

Fig. 8. Seismic section IT17RS316 in seconds Two-Way travel Time (TWT). a) uninterpreted section; b) interpreted section. The contouritic mounds indicated in Fig. 6 are identified as M2-6 and the scarps as S1-3. Location of the seismic section is shown in Fig. 2.

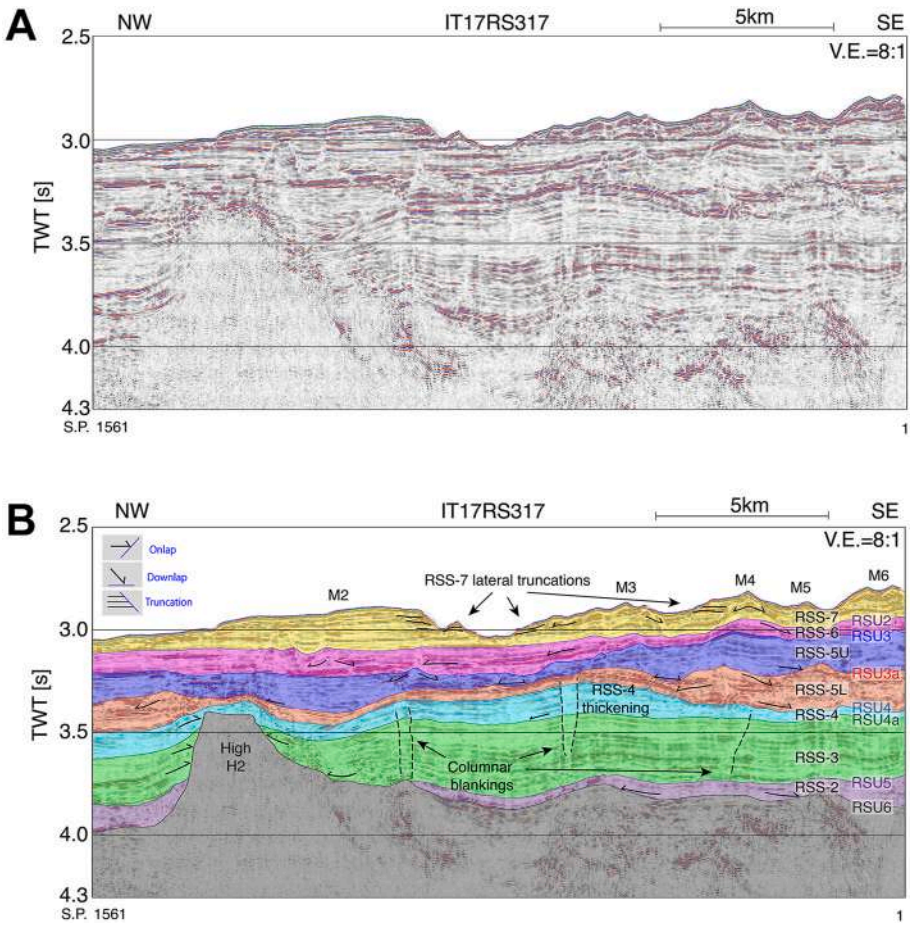

Fig. 9. Seismic section IT17RS317 on the continental rise in seconds Two-Way travel Time (TWT). a) uninterpreted section; b) interpreted section. M2 to M6 correspond to mounds localized in Fig. 6. Location of the section is shown in Fig. 2.

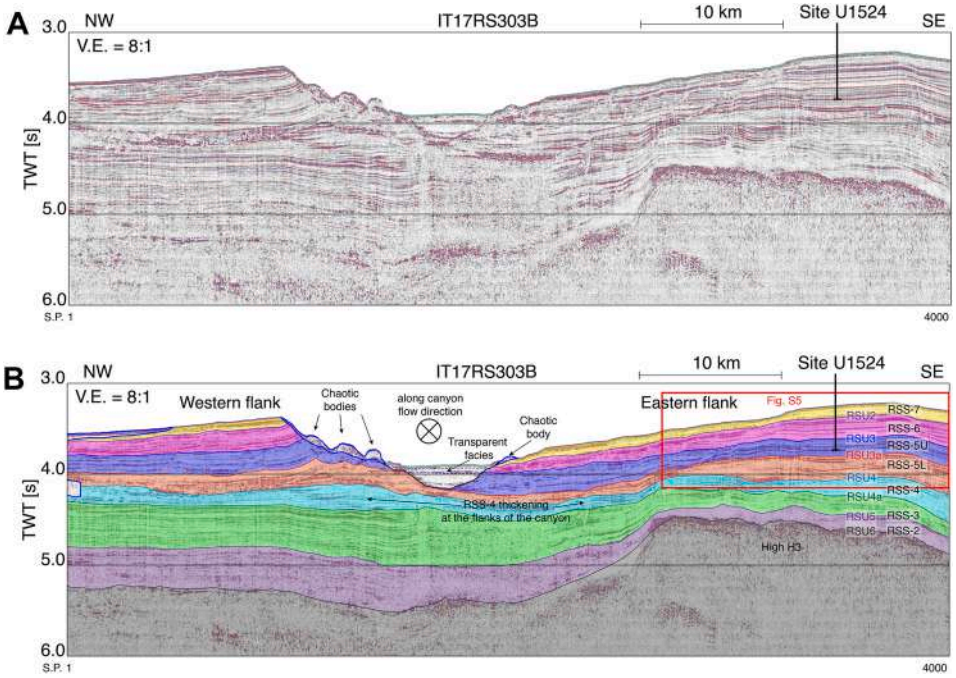

Fig. 10. Seismic section IT17RS303B in seconds Two-Way travel Time (TWT) showing the Hillary Canyon. a) uninterpreted section; b) interpreted section. Location of Site U1524 of the International Ocean Discovery Program (IODP) is indicated. Note the asymmetry of the two flanks. Location of the section is shown in Fig. 2.

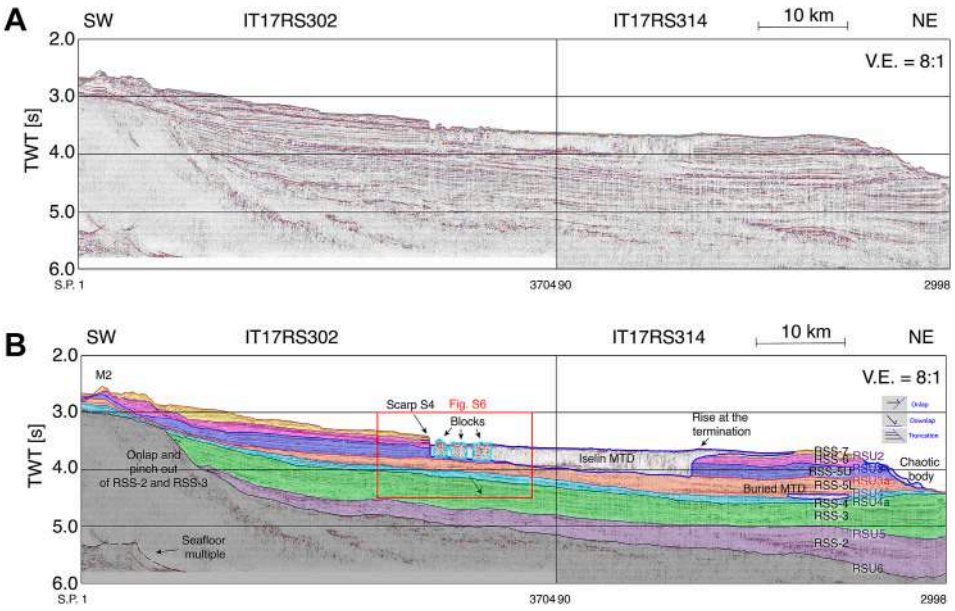

Fig. 11. Seismic sections IT17RS302 and IT17RS314 in seconds Two-Way travel Time (TWT) showing the Iselin Mass Transport Deposit (Iselin MTD) and one of the two buried MTDs. a) uninterpreted section; b) interpreted section. Location of the section is shown in Fig. 2.

and shape to the ones identified in the bathymetry, are found close to the base of the continental slope, whereas in the other deeper sectors the reflections of RSS-4 are generally sub-parallel and sub-horizontal. RSS-4 thins toward the edge of the Iselin Bank where it terminates in downlap on RSU4a (Fig. 7). RSS-4 thickens at both levees of the Hillary Canyon (Fig. 10). Two lensoidal units showing acoustically transparent to chaotic facies are found between the upper part of RSS-4 and the lower part of RSS-5. They cut the continuity of the unconformity RSU4, which is the low angle truncational, high-amplitude and elsewhere laterally continuous reflection at the top of RSS-4. These lensoidal chaotic units have a thickness of around 0.1 s in TWT, that is equivalent to around 80 m (Figs. S4 and 11).

3.2.1.5. RSS-5. Similarly to RSS-4, RSS-5 shows variations in thickness and mounds with upward convex internal reflections, but the relief is more pronounced, with the growth of M2 (Figs. 8 and S3), M4 and M5 (Fig. 9), whose morphology is preserved and enhanced in the overlying sedimentary sequences. RSS-5 represents the main growth phase of the levees of the Hillary Canyon (Fig. 10), whose high lateral continuity reflections are interrupted or truncated in correspondence of the transparent or chaotic with cut-and-fill structures of the thalweg. On the steeper western levee, the reflections terminate abruptly against the canyon cut (Fig. 10) and three bodies with transparent/chaotic facies can be identified, whereas on the eastern levee, the reflections are truncated by the canyon at lower angle. Within the eastern levee, the reflections are sub-parallel but undulated (Fig. S5). This sequence is divided by RSU3a into RSS-5 lower and upper.

RSS-5 lower is thicker on the levees of the Hillary Canyon and thins toward the canyon thalweg (Fig. 10), while it has a mounded character near the Iselin Bank edge where reflections downlap on RSU4 to the west of H1 (Fig. 7). Reflections then pinch-out and are sharply cut by the scarp S2, resulting in a mound (M7) partially incomplete due to truncation (Fig. 7).

The bottom and top boundary of RSS-5 lower are RSU4 and RSU3a, respectively, which represent mainly downlap surfaces, though they are onlap surfaces on the flanks of the mounds (Figs. 8 and S3). RSU3a largely coincides with the basal surface of a prominent transparent to chaotic body with discontinuous, cross-cutting, low amplitude reflections (Iselin MTD, Fig. 11) that involves sequence RSS-5 upper and all the sequences above it up to the seafloor. This body is around 0.3 s TWT thick, equivalent to about 240 m. Immersed, but outcropping within this chaotic body, close to the scarp S4, there are three units about 1 km wide and 0.3 s TWT thick, characterized by high-amplitude stratified reflections, that are slightly deformed but laterally continuous (blocks in Figs. 11 and S6).

RSS-5 upper shows more mounds forming close to the base of the continental slope with downlap on RSU3a (M3-M6 in Figs. 8–9). On the Iselin Bank, the reflections of RSS-5 upper pinch out in correspondence of M7 and are truncated by the scarp S2 (Fig. 7). The upper boundary of RSS-5 upper is RSU3, a high-amplitude and laterally continuous reflection that is a low angle truncation surface in the rise, slope and shelf of the Iselin Bank and on the levees of the Hillary Canyon.

3.2.1.6. RSS-6. RSS-6 is thinner above the mounds identified in RSS-5, filling and smoothing the paleo-seafloor morphology (Figs. 8, 9, S3). The same filling characteristics are observed in the north-western part of the continental rise, to the east of S5 (Fig. S4). At the base of the continental slope, in the depression between M2 and the continental slope, a channel-like feature cuts the top of RSS-6 (Fig. 7). On the Iselin Bank RSS-6 has sub-parallel reflections but shows some onlap terminations on RSU3 west of H1 (Fig. 7), indicative of a filling of the depression. The top boundary of RSS-6 is RSU2, a high-amplitude reflection with high lateral continuity that represents a low angle truncation surface both in the deep and shallow areas.

3.2.1.7. RSS-7. The main characteristic of this seismic sequence is the very pronounced thickness variation close to the base of the continental slope, above the underlying morphology partially smoothed by RSS-6 (Figs. 8 and 9). RSS-7 generates most of the relief of the present seafloor. The RSS-7 reflections are often laterally truncated by scarps on the seafloor (Fig. S3, and scarps cutting the mounds in Fig. 9) leading to particularly steep flanks of the mounds. M1 on the Iselin Bank is distinctly growing during the deposition of RSS-7, with reflections that are upward convex (Fig. 7). In the distal part of the continental slope, the reflections are sub-parallel, with the exception of the Iselin MTD. The RSS-7 reflections are laterally truncated by the Hillary Canyon (Fig. 10).

3.3. Water mass interactions

The simulated temperature across Transect 10 shows that three main water masses strongly interact at the continental margin in the ODYSSEA area: the AASW, the RSBW and the CDW (Fig. 5f). The AASW (with potential temperature $< 0\,^{\circ}C$, often close to $-1\,^{\circ}C$, and salinity < 34.40) flows in the upper layer, until about 100–150 m depth. The CTD profiles acquired at stations 9 and 10 during the 2017 campaign confirm these properties (Fig. 5a and b). The RSBW (with temperature below 0 °C, or even below the surface freezing point of -1.9° and salinity around 34.60–34.70) descends in the bottom layer downslope from the upper to the deep continental margin (Fig. 5f). The cascading of the modified RSBW is observed by CTD casts at stations 9 and 10, showing an increase in velocity from approximately 1500 m depth and 1900 m depth, and is also captured by the numerical model simulations (Fig. 5e and f). This coincides with the decrease in temperature measured from 1200 m depth and 1700 m depth in CTD 9 and 10, respectively (Fig. 5a). Thickness of the cool RSBW layer agrees with the simulated thickness of RSBW on Transect 10 (Fig. 5f). Descending flow locally triggers an increase in turbidity (Fig. 5c) as well as a speed increase up to 0.25 m/s (Fig. 5d), well visible in the simulated horizontal velocities (Fig. 5e and g). A local maximum in the bottom velocities results from the strong downslope flow, and occasional cascading of the RSBW on the western flank of the Hillary Canyon (looking seaward). The simulation suggests that although recurrent, the cascading of the RSBW is not a continuous process (Supplementary Video 01). The CDW (with relatively high core temperature, 0.50 °C–1.50 °C and higher salinity, 34.50–34.70) flows at depths below 300 m in between the ASSW and the RSBW (Fig. 5a, b, and 5f). The deep part of the CDW between 1000 and 1500 m depth flows along-slope as part of the ASC (Fig. 5e). A thin CDW layer intrudes onto the continental shelf at shallower depths (<200 m) (Fig. 5f). CTD stations, although slightly offshore, captured the local CDW temperature and salinity maximum at around 300 m depth (Fig. 5a and b). Intrusion of the CDW into the shelf is triggered by both the downslope flow of RSBW and the meandering of the geostrophically-adjusted ASC along the Iselin Bank (Supplementary Videos 02 and 05). Thus, as for the RSBW descending flow, the intrusion of CDW is episodic even if often recurrent in that area (Supplementary Video 01). CTD 9 shows that local mixing occurs between AASW and CDW and is potentially due to the meandering of the ASC until about 400 m depth. Turbidity is high in the surface to sub-surface layers (Fig. 5c) due to the biological activity, where also mesoscale eddy activity was recorded by the vmADCP data (Fig. 5e top). In the upper continental slope, turbidity increases gradually at CTD 9 from about 1000 m depth triggered by both the ASC and by the cascading of the RSBW which locally mixes with the CDW (Fig. 5a, b and 5f).

Supplementary video related to this article can be found at https://doi.org/10.1016/j.dsr.2021.103606

The ASC flows northward along the Iselin Bank at intermediate depths (1000 m–1500 m) with maximum velocities reached when bathymetry locally changes orientation and presents strong curvature, i.e. in the Hillary Canyon (Fig. 6) and slightly northward of the ODYSSEA area (Fig. 5h and Fig. S2f). Occurrences of simulated horizontal velocities larger than 25 cm/s (average velocity of the ASC, Fig. 5h) shows that this route corresponds to the preferential ASC pathway along the Iselin Bank. The ASC intensity, however, fluctuates through time and it is influenced by the mesoscale processes (Supplementary Video 02).

Three main routes of the descending shelf water emerge from the simulation (Fig. 5h). The along-slope Route 1, which comprises the largest volume of the shelf water, is connected with the geostrophic adjustment, slowly descending due to the bottom friction. It strongly conserves its potential vorticity, which allows it to reach a long distance from the spillover point near the shelf break. Route 2 is again more or less adjusted, but at deeper depths, it detaches from the main geostrophic flow due to baroclinic instability, descending along the left side of the Hillary canyon. Route 3 follows Route 2, but is more variable and occurs in the simulation when instabilities are triggered, allowing the flow to reach the deeper abyssal part of the basin. The model only partially resolves this process because of relatively coarse horizontal and vertical grid resolution as well as the lack of non-hydrostatic components in the simulated dynamics. Route 3 is connected to the intense cascading process that is much more episodic than the other two.

Route 2 and Route 3 originate from the downslope flow of RSBW that occurs on the western flank of the Hillary Canyon. Cascading of the RSBW can thus be tracked through the study area (Transect 11, Fig. 5h) and is clearly visible in the bottom velocities (Supplementary Fig. S2f). Often a strong velocity current detaches from the main geostrophic flow (Route 2) and proceeds northward, following the trajectory of Transect 11 (Figs. 5h and S2g) up to the northernmost part of the study area (Route 3). Temperature and velocity fields show very well the downslope flow that locally feeds the AABW core (Supplementary Fig. S2a, S2b and S2c). As for Transect 10, in the ODYSSEA area, downslope flow occurs recurrently through time but is not continuous (see Supplementary Videos 03, 04, 05 & 06) according to dynamical behavior of such bottom trapped gravity currents. Upslope flow of CDW occurs mostly on the eastern flank of the Hillary Canyon (Supplementary Video 06, southernmost edge of the video) flowing mostly southward from the Ross Sea Gyre (Fig. 5e). This overall behavior is supported by previous studies showing that the Hillary Canyon is one of the few places of the Ross Sea where bathymetric characteristics and oceanographic conditions allow both the downslope flow of the dense waters from the adjacent continental shelf and the upslope flow of the CDW (Jacobs et al., 1992; Walker et al., 2007; Dinniman et al., 2011; Tinto et al., 2019).

Supplementary video related to this article can be found at https://doi.org/10.1016/j.dsr.2021.103606

Despite the limitation (15 years spanning from 1999 to 2014 and starting from a perpetual 1998 year), the overall behavior from the simulation agrees remarkably well with measurements collected in February 2017, although those measurements represent a snapshot of austral summer conditions. Main dynamical processes characterizing the whole Ross Sea, as well as the characteristics of the evolution of water masses, are consistent with the phenomenological model of this southern area and very well reproduced (e.g. Dinniman et al., 2011). This allows us to use this modern setting and a random year through the transient simulation to discuss the general characteristics of the water masses in the study area. Furthermore, both the measurements collected during the cruise and the simulation match with existing oceanographic datasets in the area (e.g. CLIMA Project, Budillon and Spezie, 2000; Orsi and Wiederwohl, 2009). This gives confidence to use simulated and measured oceanic conditions as a support for discussing long-term interactions between the main water masses and the geological and geophysical analysis of the area.

4. Discussion

4.1. Age model-seismic profile integration

At IODP Site U1523, the seismic velocity model resulting from the combination of PWC with DSI measures gives a reliable time-depth conversion (Fig. 4) and is consistent with that obtained from the crossing section IT94AR127A. Time-depth conversion suggests a good matching between the hiatus from 3 to 5 Ma to 8.5 Ma and the mapped RSU3.

On the contrary, at IODP Site U1524 we had only velocities measured on board on section halves, which show average values lower than 1500 m/s still around 250 mbsf, attributed to the high diatom content of the drilled sediments (McKay et al., 2019). We think that such velocities severely underestimate the values of the undisturbed sediment, as sediment decompaction is known to give values lower than those in situ (Blum, 1997; Sauermilch et al., 2019). In fact, velocities at site U1524 are definitively low compared with those from sonic log in

similar settings (e.g. sites 1095 and 1096 of the ODP Leg 178, in a contourite drift succession with comparable high diatom content, above the diagenetic front, Volpi et al., 2001). We thus propose an alternative velocity model, increasing linearly from 1500 m/s at seafloor to 2000 m/s at 400 mbsf, which allows a good match between the hiatus from 4.5 to 8 Ma and the correlated RSU3, and between the hiatus from about 3 to 4 Ma and another intermediate seismic unconformity (that cannot be correlated through all the dataset) crossing the Site U1524 at about 3550 ms TWT (Figs. 4 and S5). The discrepancies between this alternative model and PWC velocities are around 50 ms TWT at a depth of 350 mbsf, and do not affect the interpretation at the scale and resolution we are looking at.

For the unconformities RSU7, 6, 5 and 4a we adopt the ages attributed in previous works (Table 1). For RSU4, intercepted at Site U1523 below the maximum depth reached by the age model, we extrapolate an age of about 14.5 Ma, consistent with the age obtained by previous works at other drill sites on the continental shelf (Table 1). RSU3a, intercepted only at Site U1523, has an age of around 11 Ma, whereas at Site U1524 the extrapolation of the uncertain age model below 340 mbsf (Fig. 4) suggests an age of about 9.5 Ma. For RSU3, Brancolini et al. (1995b) attributed to it an age of 10 Ma matching with a lowstand in the eustatic sea level curve from Haq et al. (1987), but according to our correlation it corresponds to a hiatus from 8 to 4.5 Ma at Site U1524 and from 8.5 Ma to 3–5 Ma at Site U1523 (McKay et al., 2019), and we thus suggest an age of about 8–5 Ma. RSU2 is intersected at both IODP sites U1524 and U1523 with an age around 2.5 Ma (Table 1, Fig. 4).

4.2. Bottom current control on sedimentary features

In seismic profiles the action of bottom currents is principally indicated by the presence of sediment drifts, that are characterized by thickness changes in the seismic sequences produced by mounds whose internal reflections have an upward convex shape and downlap terminations (Rebesco and Stow, 2001). Integrated with multibeam bathymetry, these data provide a fundamental information to discriminate sediment drifts from deposits produced by down-slope flow: contourite drifts usually have a characteristic elongation subparallel or oblique with respect to the bottom current and continental slope direction (Rebesco et al., 2014). In some cases drifts perpendicular to a margin can result, according to Faugères et al. (1999), from progradation in response to a change in the margin's trend (e.g. Eirik drift) or interaction between surface and bottom currents (e.g. Blake–Bahama drifts). By looking at the external shape and internal geometry of the sedimentary bodies west of the Hillary Canyon we identify all the characteristics indicating the action of bottom currents (i.e. upward convex shape of the reflections, downalp terminations, elongation mainly sub-parallel to the continental slope direction). Though two of them (M5-6) are almost perpendicular to the general trend of the margin, we observe that the mounds lie in correspondence of a change in the margin's trend and may have possibly been produced by progradation in response to this particular setting. In support of the morpho-bathymetric and structural evidence, surface sediment cores collected in this area clearly indicate an overall deposition under contour currents (Lucchi et al., 2019) with bioturbated (warm conditions) and finely laminated sediments (cold conditions) indicating persistent shear strength conditions at the sea bottom, similar to what described in other Antarctic margins (Lucchi et al., 2002, 2007). This depositional imprint is maintained in the deeper stratigraphic sequence as indicated by the sediment record recovered at the IODP Site U1523 on the Iselin Bank. Here the main sedimentary facies is made of diatom-bearing, structureless to laminated sediments, with planar to wavy sand and silt laminae with dispersed clasts tentatively interpreted as ice -proximal to ice-distal glaciomarine sedimentation with winnowing by bottom currents (McKay et al., 2019). Ongoing analysis on the ODYSSEA surface sediment cores and IODP sites U1523 and U1524 will provide more information about the strength and character change of bottom current through time on the two sides of the Hillary Canyon.

Towards the shelf edge, this drift comprises mounds M1 (Fig. 6) and M7 (Fig. 7) that are similar, both in seismic and geometrical characteristics, to other small-size sediment drifts identified elsewhere in various settings at different latitudes (Rebesco et al., 2014).

The mounds identified on the continental rise (M2-6) are mostly subparallel or oblique to the local SW-NE direction of the southernmost part of the Iselin Bank (Figs. 1 and 6, Table 2): if these mounds were controlled by the action of turbidite flow only, they would be elongated perpendicularly to the continental slope. Their internal geometry, also resembles that of other larger sediment drifts identified in Antarctica (e.g. Rebesco et al., 2002, 2007; Scheuer et al., 2006; Kim et al., 2018) and elsewhere (e.g. Ceramicola et al., 2001; Hernández-Molina et al., 2011, 2016). Mound M2 is elongated in the same direction of the H2 high and grown on its top, and shows an asymmetrical geometry resulting from a condensed succession and pronounced downlap on the steeper flank and well stratified, laterally continuous reflections on the gentler flank, which is typical for contourite drifts (Rebesco and Stow, 2001). Consequently, high H2 may have represented an elevated area that deviated the bottom currents and favored the deposition on its top. In alternative, M2 and the other mounds could be interpreted as turbiditic levees, which are characterized by a similar geometrical configuration. However, if this was the case, we expect all of them to be elongated perpendicularly to the continental slope direction. Adding to this, since Coriolis force in the southern hemisphere is directed to the left, M2 would develop as the levee of the channel located between M2 and M3 (Fig. 8). But in this case it would have an eastern steeper flank (with pronounced downlap towards the channel) and a western gentler flank. This is the opposite of what can be observed in the seismic sequences within M2 below RSS-7, which is cut by the detachment scarp S3. Therefore, the asymmetric geometry of M2 is compatible with a dominant action of along-slope currents (possibly with two cores, one on each flank, one stronger than the other), but not much with the action of turbidity flows alone. Adding to this, the elevation of M2 with respect to the channel between M2 and M3 (over 300 m) would be quite high to allow the suspended sediment transported by turbidity flows to reach its top and produce such an evident growth. We thus infer that all these mounds are controlled by the action of bottom currents that play a key role in sediment transport and deposition. Indeed, both measured and simulated bottom velocities within the ASC are recurrently larger than or around 20 cm/s (Fig. 5d and Fig. S2f) in the intermediate to lower continental slope. Measurements over a drift in the Antarctic Peninsula suggest that most of the time, bottom currents are too weak to re-distribute fine sediments and thus, only bottom velocities larger than about 20 cm/s can transport sediment over less energetic areas (Giorgetti et al., 2003). The ASC is a robust oceanographic feature and we expect its intensity to vary through time. In the Ross Sea sector, the ASC is fed by the southern branch of the Ross Sea gyre. Coupled Miocene numerical simulations show that the Ross Sea gyre is a robust oceanographic feature even if paleo-bathymetry differed from present-day one and that its flow was more intense than nowadays leading to stronger AABW formation (e.g. Huang et al., 2017). Changes in bathymetry in the Weddell Sea induced a northward shift of the Weddell Sea gyre through time and an overall decrease of its intensity (e.g. Fig. 5 in Colleoni et al., 2018a,b). Given the evolution of the Ross Sea continental margin, we expect similar changes for the Ross Sea gyre, though perhaps less pronounced than in the Weddell Sea.

Mounds M2-6 develop in an area where the bottom currents slow down with simulated velocities lower than 3 cm/s but can marginally reach 25 cm/s (Figs. 6 and Fig. 5h and Fig. S2f) and are bounded by the ASC along the continental slope and by the downslope flow from the Hillary Canyon (Fig. 5f). Thus the mounds develop where the bottom currents are active but are not so strong to prevent deposition. M1 and M7 developed in a similar context, but at shallower depths at the edge of the Iselin Bank (Fig. 7), where velocities slow down to 3 cm/s and less (Fig. S2f), and bounded by the ASC at intermediate depths. We note a

concentration of mounds M2-6 close to the Iselin Bank (Fig. 6) and a decreasing abundance of sediment drifts moving seawards from the continental slope and northwards from the easternmost bulge in the Iselin Bank. This is marked by a transition from prevailing thickness variations and downlapping geometries to a dominance of subparallel reflections (Fig. 11). An explanation could be that sediment supply decreased while departing from the continental slope. However, the fact that the sequences are thickening seawards (Fig. 11) means that the distance from the sediment source was not a limiting factor for the growth of mounds. A better explanation is that in these distal settings bottom currents are not strong enough to produce sediment drifts. In fact, the simulation shows decreasing velocities in correspondence with decreasing number of drifts away from the continental slope (Fig. 5h and Fig. S2f) as well as only episodic cascading of dense shelf waters along the Hillary Canyon down to that area.

Oceanographic data collected in 2017, although being a snapshot of the local austral summer condition, support our interpretation of seismic profiles and multibeam bathymetry. In particular, the increase in turbidity and current speed in proximity of the bottom layer at both CTD stations (Fig. 5c and d) suggests the availability of sediment and the presence of active bottom currents. Because of their relative position on the continental margin, CTD 9 (lower slope, higher turbidity) receives the supply of organic/inorganic suspended matter more directly than CTD 10 (rise, lower turbidity). This, combined with observed and simulated strong downslope flow at both CTD stations (Fig. 5f) and interactions with strong along-slope currents (Fig. 5e) at CTD 9 are ideal conditions for the development of sediment drifts. The split of descending waters, with Route 1 geostrophically-adjusted along the slope and Routes 2 and 3 descending and reaching the northward abyssal areas (Section 3.3), defines a zone of low velocity where sediment drifts M2-6 have developed. The persistent combination of these factors over time is deemed responsible for the development of the sediment drifts found in this area.

The seaward thickening of seismic sequences in the continental rise (Fig. 11) suggests that sediment could originate also from a different location, for example, the Hillary Canyon. In fact, the canyon occasionally funnels sediment gravity flows (downslope flow Route 3, see Section 3.3) and more regular cascading of RSBW (Route 2, section 3.3) along its western flank, leading to temporary increases of suspended sediments. We did not spot this phenomenon during the oceanographic campaign in 2017, however, the simulation shows that downslope flow is recurrent but intermittent and that, occasionally, strong cascading occurs and reaches abyssal depths (see Supplementary video 05, 06 & 07). While cascading of RSBW occurs along the western flank of the Hillary Canyon, upslope flow of CDW occurs on its eastern side (Supplementary Video 06). The overall simulated water mass behavior supports the interpretation of the asymmetrical western flank of the Hillary Canyon at about 2500–3000 m water depth (Fig. 10) as a mixed levee-drift system similar to other cases identified elsewhere in Antarctica (Kuvaas and Leitchenkov, 1992; Michels et al., 2001; Escutia et al., 2002; Rebesco et al., 2002; De Santis et al., 2003; Maldonado et al., 2005; Donda et al., 2007, 2020; Solli et al., 2007; Uenzelmann--Neben and Gohl, 2014).

Supplementary video related to this article can be found at https://doi.org/10.1016/j.dsr.2021.103606

The depositional system resulting from the association of sediment drifts and related erosional features that indicate the dominant action of along-slope bottom currents is termed as Contourite Depositional System (Stow et al., 2002; Hernàndez-Molina et al., 2003; 2008; 2009). Given the dominant control of along-slope bottom currents on sediment deposition between the Iselin Bank and the Hillary Canyon, inferred from the geometry and structure of the sedimentary bodies and supported by the evidence from the depositional record (planar to wavy sand and silt laminae in IODP Site U1523; McKay et al., 2019) that is in line with the simulated bottom velocities, we regard this area as a Contourite Depositional System, that we name ODYSSEA.

4.3. Interplay between sediment drifts and mass transport deposits

Often sediment drifts are found in association with Mass Transport Deposits (MTDs) as the formers are prone to failure because of five main factors (Laberg and Camerlenghi, 2008; Rebesco et al., 2014; and references therein): 1) their mounded geometry enhances the local gradient of the inclined continental slope, 2) their relatively high sedimentation rate and high water content causes low shear strength, 3) their low-permeability and high-porosity (especially if siliceous ooze layers are present) result in under-consolidation and excess pore pressure, 4) rapid loading (e.g. by glacigenic sediments during glacial stages) prompts liquefaction, and 5) gas charging (i.e. by migration from relatively high organic-carbon deposits associated to productive water masses) promotes fluidification.

MTDs are recognizable in cross-sectional seismic lines by the presence of seismic facies that show low-amplitude, semi-transparent to chaotic reflections (Posamentier and Kolla, 2003; Moscardelli and Wood, 2008), often bounded by steep scarps called detachment scarps. Within the ODYSSEA CDS, we identified several bodies with the same characteristics that are commonly seen in MTDs, including the presence of internally undeformed transported blocks submerged in the surrounding chaotic material (Lee et al., 2004; Moscardelli and Wood, 2008), like those that we identify close to scarp S4 (Figs. 11 and S6). While MTDs are easily identifiable by their seismic facies, the scarps can be identified not only in the seismic sections but also on the bathymetric data if the MTD is outcropping at the seafloor. The scarps we identified (S1–S5), and interpreted as detachment scarps, helped us to map the extensive MTD, that we called Iselin MTD, and the occurrence of other gravitational movements. Through the interpretation of seismic and morpho-bathymetric data that allows the identification of both CDS and MTDs, we found evidence for the presence of an interplay between sediment drifts and mass transport deposits in correspondence of the ODYSSEA CDS.

An interplay between MTDs and contourites is observed at many sites, including the continental rise of the Antarctic Peninsula (Rebesco et al., 1998, 2002; Dowdeswell et al., 2004; Amblas et al., 2006; Diviacco et al., 2006; Rebesco and Camerlenghi, 2008), Wilkes Land (Donda et al., 2008) and the Ross Sea (Kim et al., 2018). Also in the study area, we notice that the Iselin MTD and the smaller buried MTDs involve the sequences from RSS-4 to RSS-7, which are the sequences showing thickness variations that we relate to bottom current activity (Figs. 11 and S4). Conversely, no MTDs are identified in the seismic sequences RSS2-3 preceding the development of the contouritic mounds in this area. We also observe that the detachment scarp S3 laterally cuts RSS-7 (Fig. S3), that is the sequence showing the highest thickness increase in correspondence of the mound M2. In addition, the chaotic facies at the base of the continental slope in RSS-4 is spatially associated with the overlying detachment scarps S1 and S2. These detachment scarps also develop in correspondence with the seaward side of mound M7 (Fig. 7). Finally, the overall abundance of detachment scarps in the multibeam bathymetry between the Iselin Bank and the Hillary Canyon (Fig. 6) highlights the abundance of gravity-influenced movements in the ODYSSEA CDS. Therefore, MTDs and detachment scarps are frequent where seismic profiles show the control of bottom currents on sediment deposition. We also notice some columnar blankings on the continental rise (Fig. 9) that may correspond to fluid escape features (pipes). The MTDs that we observe along smooth slopes could have been favored by fluidification above the pipes similarly to what happened in the southern Scotia Sea (Somoza et al., 2019). The fact that the reflectors inside the undeformed blocks are sub-parallel to the seabed may indeed suggest sliding (creeping) within a fluidized mass and not rotation by gravitational falling. Nevertheless, the fact that we do not identify any specific columnar blanking right below the MTD (Fig. 11) and that no MTDs are identified in the seismic sequences preceding the development of the contouritic mounds corroborate our interpretation that it is the association with contourites that mainly control the development of the observed mass failures.

4.4. Evolution of the depositional system

The preliminary age model of drill sites U1523 and U1524 (McKay et al., 2019) and the thickness of the seismic sequences show that the sedimentation rate on the continental shelf of the Iselin Bank (about 15 m/My at Site U1523) is generally lower with respect to that of the continental rise, west to the Hillary Canyon at the scale of million years (about 55 m/My at Site U1524). Indeed, the Iselin Bank is expected to be in a distal location from sediments supplied by the ice sheet. During maximum advances, such as during the LGM, the ice sheet expanded almost until the Ross Sea continental shelf edge, but did not expand onto the Iselin Bank sector, where only current residual lag are found

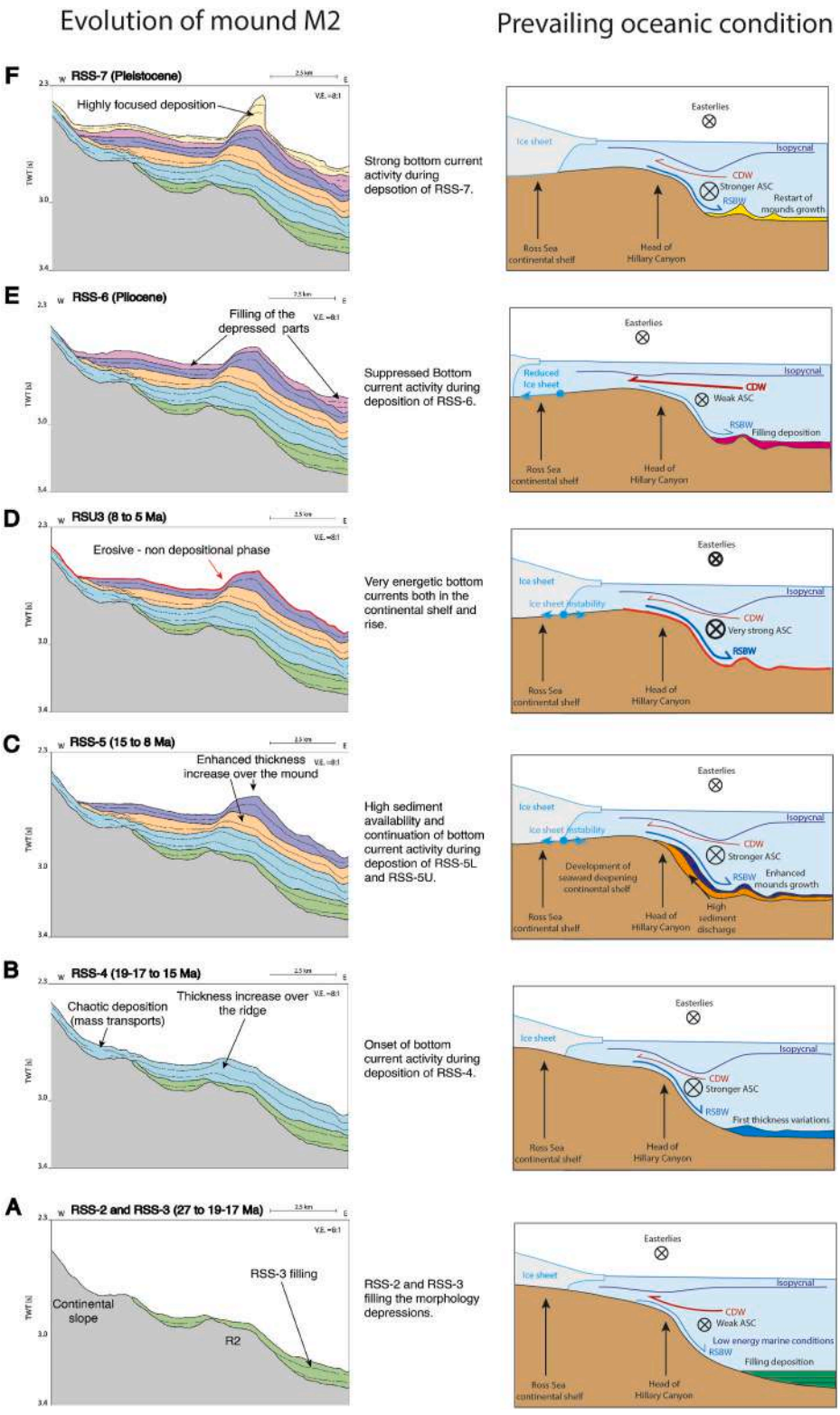

Fig. 12. Hypothesized evolution of the mound M2 (left) and associated prevailing oceanic conditions (right). Vertical scale in the left part is seconds Two-Way travel Time. ASC: Antarctic Slope Current. CDW: Circumpolar Deep Water. RSBW: Ross Sea Bottom Water.

(Taviani et al., 1993; Halberstadt et al., 2016; Anderson et al., 2019). The lack of clear glacial erosional and depositional features, as well as the occurrence of sediment-drift features forming behind a morphological high, already visible in the RSS-3 (Fig. 3), indicate that the Iselin Bank was mostly dominated by bottom currents, as today, rather than by subglacial overriding during the last glacial cycle and probably also during older cycles. The material recovered at DSDP Site 270, together with seismic data, indicate at RSS-1 time (>27 Ma) the presence of some glaciers and local ice caps covering possibly slightly emerged reliefs in the Ross Sea (Hayes and Frakes, 1975; Brancolini et al., 1995b; De Santis et al., 1995; Bart and De Santis, 2012; Kulhanek et al., 2019).

Ice was locally grounding in the Ross Sea south of the Iselin Bank since early Miocene (~23 Ma) (Anderson and Bartek, 1992; De Santis et al., 1995) and glaciers terminating at the margins of the Glomar Challenger and Pennell Basins were also feeding the continental rise with glaciomarine sediments delivered through the Hillary Canyon, where large sedimentary mounds grew during the mid to late Miocene (De Santis et al., 1999; Pérez et al., 2021a). This glaciomarine deposition of sediment, delivered by the regional ice caps covering the adjacent continental shelf, is reflected in the filling characteristic and internal geometry of RSS-2 (>27 - 18 Ma) and RSS-3 (18 - 17 Ma) in the study area (Figs. 1, 9 and 112A). Overall, RSS-2 and RSS-3 are the thickest sequences in the continental rise and we infer that this is an expression of the intense erosion of the continental shelf in the Ross Sea.

The action of bottom currents becomes evident both on the continental shelf edge and continental rise only starting with the deposition of RSS-4 (17–14.5 Ma) (Figs. 1, 7 and 82B). The simultaneous inception of intense downslope flow of turbidity currents and/or dense water masses through the Hillary Canyon, as shown by the thickening of RSS-4 at its levees (Fig. 10), supports our hypothesis that the bottom current activity in the area of the continental rise is connected with the downslope flow of dense shelf waters (see Section 3.3; e.g. Gales et al., 2021). Indeed, both sediments and dense water masses were funneled by the Hillary Canyon, but we think that it was the outflow of dense shelf waters to trigger the development of the mounds because a great amount of sediment was delivered to the continental rise also prior to RSS-4, as shown by the higher thickness of RSS-2 and RSS-3 in the continental rise than on the continental shelf. But it was with the establishment of an intense enough bottom current circulation that the sediment drifts started to more substantially grow after RSU4a, and at least until RSU3.

The growth of the mounds indeed appears to be enhanced during RSS-5 (14.5–8 Ma) (Figs. 1, 8 and 92C) and this may reflect an increased sediment discharge from the shelf to the continental rise, via the Hillary Canyon and possibly via other canyons along the Ross Sea southeastern margin. We would also expect a high availability of biogenic suspended material keeping into account the biologically sourced high depositional rates at Site U1524 (McKay et al., 2019). This hypothesis agrees with the observed progradation of the Ross Sea continental slope sustaining high sediment supply to the continental rise during RSS-5 deposition (De Santis et al., 1999; Kim et al., 2018). Indeed, after the Middle Miocene Climate Transition (around 14 Ma; Flower and Kennett, 1993) there were major expansions of grounded ice sheets over the continental shelf and the development of cross-shelf ice streams, associated with RSU4, that could have delivered a greater amount of sediment to the head of the Hillary Canyon (Anderson et al., 2019; Levy et al., 2019). RSU4 (and perhaps also RSU3a) may possibly correspond to Reflector-c in Weddell and Scotia Sea, which represents either a period of non-deposition, a highly condensed sequence, or possibly even the result of sediment winnowing or erosion at some time between 14.2 and 8.4 Ma related to a major change in the regional oceanic circulation pattern (Pérez et al., 2021b). This phase of mounds growth in the Ross Sea, given by the combination of sediment availability and bottom currents, is interrupted by RSU3, coinciding with a hiatus extending from 8 to 4.5 Ma at IODP Site U1524, from 8 to 5-3 Ma at Site U1523 and from 8 to 5.5 My at Site U1522 (McKay et al., 2019) (Fig. 12 D). At IODP Site U1522, on the inner continental shelf, this hiatus was probably generated by erosion from ice sheet advances and retreats, which resulted in important erosion of previously deposited sediments (McKay et al., 2019). Sea surface temperature records show that at the end of the Miocene a global cooling (Herbert et al., 2016), likely related to further growth of the Antarctic Ice Sheet. We do not have direct stratigraphic information from drilling about the period between 8 and 5 Ma but, according to seismic data, overdeepening of the shelf and a landward deepening profile became established on the continental shelf, particularly in the eastern Ross Sea (De Santis et al., 1999). This new configuration likely led to a greater sensitivity of the ice sheet to changes in oceanic conditions (Colleoni et al., 2018a,b), that resulted in more frequent and larger advances/retreats leading to the hiatus observed at IODP Site U1522, and to a shift in the formation processes of dense water masses on the continental shelf. Indeed, a landward deepening continental shelf makes ice sheets more unstable according to the mechanism of Marine Ice Sheet Instability whereby a short-term increased oceanic heat flux at the continental shelf edge can trigger an accelerated runaway ice sheet retreat (Thomas and Bentley, 1978; Schoof, 2007; DeConto and Pollard, 2016). On the contrary, IODP sites U1524 and U1523 were never overridden by a grounded ice sheet and a process other than glacial erosion is required to explain hiatus formation. By taking into account the position of these two sites, in the outer part of the Iselin Bank and in the continental rise close to the Hillary Canyon, this hiatus was likely produced during a period of enhanced bottom currents and sediment bypassing/refocussing, possibly related to a stronger ASC or stronger production and cascading of dense water, which can occur simultaneously and are not easily distinguishable. IODP Site U1524, located on top of the Hillary Canyon eastern levee, was possibly exposed to faster bottom currents than the deeper surroundings, although this is not the case in a modern setting (Fig. 5h and Fig. S2f). The onlap terminations to the east of IODP Site U1524 (Fig. S5) probably record these faster bottom currents on the top of the levee that allowed deposition only in the adjacent deeper parts away from the Hillary Canyon. The fact that a hiatus with a similar timing is recorded also at Site U1523 suggests that the intense bottom water circulation in the continental rise, related to the outflow of dense shelf waters, was accompanied by a vigorous circulation on the Iselin Bank, that we infer to be related to a strengthening of the ASC during a phase of cooling (Herbert et al., 2016). During full glacial periods, the Ross Sea continental shelf is fully covered by an ice sheet (e.g. The RAISED Consortium, 2014; Prothro et al., 2020). As a consequence, the present-day circulation, as we know it, vanishes. However the ASC still exists. Given the lack of continental shelf circulation and the presence of the Antarctic ice sheet grounding line close to the shelf edge, the ASC is restricted to a narrower area of the slope, with less possibilities of energy dissipation with water masses exchanges across the continental shelf. This would induce an intensification of the ASC. This process could be further enhanced by the strengthening of the westerly and easterly winds (e.g. Kohfeld et al., 2013). However, this aspect is model-dependent and there is no clear consensus about the behavior of those winds during glacials, as for example the Last Glacial Maximum (e.g. Chavaillaz et al., 2013). Vice versa, during interglacials, the westerly winds and the easterly winds are shifted poleward (e.g. Lamy et al., 2010). As in the case of the LGM, it is not clear if they also intensify and this feature is largely model-dependent (e.g. Zhang et al., 2013). But as the continental shelf is ice-sheet free during interglacials, circulation would look like the present-day one, with slightly more warm water intrusions. We hypothesise that across shelf exchanges would cause a decrease in the ASC intensity as they resume.

CDW inflow and RSBW outflow are controlled by the strength of the ASC, which in turns is modulated by the Easterly winds. Nowadays, when the Easterly winds shift over the continental shelf, the ASC is weak, which allows CDW intrusions on the continental shelf and prevents downslope flow of dense shelf waters (Schmidtko et al., 2014). When strong Easterly winds are located above the continental shelf break (e.g. Ross Sea), the ASC is strong and assumes a V-shape visible in isopycnals, which reduces the CDW inflow but allows for more frequent

RSBW outflows. By analogy, during cooling periods, bottom water formation is likely enhanced in relation to increased sea ice production and Easterly winds probably strengthen, which favors stronger downslope flow (e.g. Levy et al., 2019). During warming periods it is assumed to work in the opposite direction (e.g. interglacials or future warming, Spence et al., 2014).

Our data suggest that the erosive phase coinciding with RSU3 ended at about 4.5 Ma, that corresponds to the onset of a prolonged interval during which a reduction in ice sheet volume is recorded at Site AND-1B with 80 m of silica deposition between 4.6 and 3.4 Ma (Naish et al., 2009; McKay et al., 2012). Other records suggest during this period a warmer than present climate with reduced sea ice extent and production (Whitehead et al., 2005; Escutia et al., 2009; McKay et al., 2012; Taylor-Silva and Riesselman, 2018) as well as enhanced calving of icebergs during ice-sheet margin retreat (Cook et al., 2013; Patterson et al., 2014). The deposition of RSS-6, happening between 4.5 and 2.5 Ma, during this warmer period, is characterized by a slow growth of mounds and by smoothing of underlying morphology (Figs. 8 and 12E). We infer that the change shown by RSS-6 reflects a substantial decrease in bottom currents activity rather than sediment availability as, indeed, deposition is still happening but it is not focused on the top of the mounds. This scenario implies to us a weakening of the ASC and thus stronger CDW intrusions on the continental shelf and a substantial reduction in downslope flow of RSBW. The result is an overall reduction in bottom currents intensity in the continental rise but also at shallower depths (e.g. over the Iselin Bank, around 600–800 m depth) where ASC was operating. However, we cannot completely exclude on the basis of the seismics only that the sediment supply decreased during the deposition of RSS-6. A decrease of glacial material delivered at the continental rise is also possible because the RSS-6 sequence corresponds to the formation of a shelf margin wedge pinching out the base of the slope (De Santis et al., 1999; Kim et al., 2018; Bart 2001) and to an overall warm climate interval, with reduced ice volume (Miller et al., 2012). We also recognize that each of the stages that we describe had several glacial and inter-glacial episodes that caused differences in sediment supply to the margin, i.e. probably higher sediment delivery during times when grounded ice was near the shelf break and times when the margin was sediment starved. However, the time scale of our data allows only to discuss about mediated conditions useful to provide a frame for further analysis of the IODP Expedition 374 cores, which will have the resolution to distinguish these differences.

The warmer period is followed by a sea ice production increase culminating at 2.6 Ma (Hillenbrand and Cortese, 2006; McKay et al., 2012; Patterson et al., 2014). At the same time the carbon and nitrogen isotopes (d13C and d15N) in AND-1B after 2.6 Ma record values similar to modern ones in the central Ross Sea Polynya indicative of an increased mixing related to the deep-water formation (McKay et al., 2012). The growth of contouritic mounds within RSS-7 (Pleistocene) against the flank of the Iselin Bank (Figs. 8 and 12F) indicates resumption of intense bottom water circulation along the continental rise. Site U1524 records a hiatus between 2 and 2.5 Ma and Site U1523 shows a decrease in sediment rate, possibly coinciding as well with enhanced bottom current strength and water column ventilation. At the same time, the deposition of RSS-7 starts when the AND-1B, ODP Leg 178 and IODP Expedition 318 sites record a new phase of cooling inducing an expansion of a more persistent seasonal sea ice cover at 2.6 Ma, after the mid-Pliocene Warm Period, that could explain the increased bottom currents strength. The high amplitude of RSS-7 reflections suggests the stratification from deposition of different lithologies, possibly related to the occurrence of episodic input of terrigenous material to the continental rise and/or intensification of bottom current activity. On the Iselin Bank these changes in bottom current strength are not so evident from the geometry of the seismic sequences, apart from the relief of mound M1 that is thicker and more developed during RSS-7 than during RSS-6. Further work on the two drills sites will possibly provide more information to support our interpretation.

5. Conclusions

The unique hydrographic and sedimentary conditions of the area between the Hillary Canyon and the Iselin Bank led to the build-up of sediment drifts and levee-drifts forming a large Contourite Depositional System (the ODYSSEA CDS) since the early stages of ice sheet development in the Ross Sea (around 17 Ma). The construction of the ODYSSEA CDS occurs along the southeastern flank of the Iselin Bank, where a deviation (northward) in the regional continental slope direction (NNW-SSE trending) and the lower intensity in bottom currents allows the sediment deposition. The sediment supply comes from the continental margin, mainly through the Hillary Canyon. Suspended sediment is entrained by bottom currents that flow along the western levee of the Hillary Canyon and along the continental slope. The activity of bottom currents at the base of the continental slope of the Iselin Bank appears related to the strong flow of dense waters through the Hillary Canyon and from the Iselin Bank itself. Oceanographic data and modeling provide evidence for the essential role of the downslope flow of dense shelf waters on the growth of the mounds on the continental rise. The combination of seismic interpretation with preliminary age models obtained from the IODP Expedition 374 drill sites allows for reconstruction of 6 main phases of the ODYSSEA CDS:

1 Deposition of the RSS-2 and RSS-3 (Late Oligocene-Early Miocene, 27 to 17 Ma): reflects low energy open marine conditions near the shelf edge of the Iselin Bank. At this time, the Hillary Canyon and its levees were not fully developed (Fig. 12A).
2 Deposition of RSS-4 (Early Miocene, 17 to 14.5 Ma): represents the onset of more active gravity flow processes through the Hillary Canyon with construction of its levees and the onset of stronger bottom currents both on the Iselin Bank and in the continental rise, with the growth of sediment drifts (Fig. 12B).
3 Deposition of RSS-5 (Middle-Late Miocene, 14.5 to 8 Ma): shows evidence of active bottom currents and of enhanced sediment supply from the shelf to the rise (Fig. 12C).
4 RSU3 (Late Miocene, 8-5 Ma): represents a highly dynamical phase with very energetic bottom currents resulting in erosion and non-deposition, coinciding with a hiatus of 8–5 Ma both in the continental shelf and rise (Fig. 12D).
5 Deposition of RSS-6 (Pliocene): reflects weaker bottom currents both on the shelf and rise, in concomitance with the warm climate phase of the mid-Pliocene Warm Period (3.3–3 Ma). We infer that the production of dense waters on the continental shelf was generally reduced and the Antarctic Slope Front was very weak (Fig. 12E).
6 Deposition of RSS-7 (Pleistocene): reflects the reinvigoration of bottom circulation, after the mid-Pliocene Warm Period, and following an increase in sea ice production and polynya regime on the continental shelf. Coincides with the onset of prevailing cold climatic conditions (Fig. 12F).

The reconstructed evolution of the depositional system highlights that bottom currents strengthen during cooling intervals and periods of glacial expansion on the continental shelf, and it weakens during warmer climate phases. The hypothesis developed in this work is intended to guide future proxy-based studies to identify similar fluctuations in water masses, currents intensity and pathways as well as to infer prevailing oceanic versus ice sheet dynamics processes on deposition during past climatic transitions of the Neogene and Quaternary. Further detailed integrations with lithological, paleontological, geochemical and petrophysical data are required to achieve this objective. The Iselin Bank, the ODYSSEA CDS and the Hillary Canyon-levees are key places to further investigate how the recorded changes in bottom current intensity relate to intrusion of relatively warm waters on the continental shelf and to ice sheet stability.

Declaration of competing interest

The authors declare that they have no known competing financial interests or personal relationships that could have appeared to influence the work reported in this paper.

Acknowledgements

The authors are grateful to the support of the captain and crew of the R/V OGS Explora during the 2017 Antarctic expedition. This project used samples and/or data provided by the International Ocean Discovery Program (IODP). We acknowledge that the Antarctic Seismic Data Library System (SDLS) allows free access to all existing MCS data in the study area. We used IHS Kingdom and Schlumberger Vista for seismic data processing and interpretation under the university grants program. Funding: this work was supported by the PNRA16_00205 ODYSSEA, PNRA16_00016 WHISPERS and the PNRA18_00002 ANTIPODE projects of the Italian National Antarctic Research Programme (PNRA), and by the ANTSSS project of Eurofleets2 EU programme (The research leading to these results has received funding from the European Union Seventh Framework Programme (FP7/2007-2013) under grant agreement n° 312762", as well as the participation of OGS). RM was funded by the Royal Society Te Apārangi NZ Marsden Fund (Grant 18- VUW-089) and the MBIE Antarctic Science Platform contract ANTA1801. We thank the three anonymous reviewers for providing helpful comments that significantly improved our work.

Appendix A. Supplementary data

Supplementary data to this article can be found online at https://doi.org/10.1016/j.dsr.2021.103606.

References

Ainley, D., Jacobs, S.S., 1981. Sea-bird affinities for ocean and ice boundaries in the Antarctic. Deep Sea Res. 28, 1173–1185. https://doi.org/10.1016/0198-0149(81)90054-6.

Amblas, D., Urgeles, R., Canals, M., Calafat, A.M., Rebesco, M., Camerlenghi, A., Estrada, F., De Batist, M., Hughes-Clarke, J.E., 2006. Relationship between continental rise development and palaeo-ice sheet dynamics, Northern Antarctic Peninsula Pacific margin. Quat. Sci. Rev. 25, 933–944. https://doi.org/10.1016/j.quascirev.2005.07.012.

Anderson, J.B., Bartek, L.R., 1992. Cenozoic glacial history of the Ross Sea revealed by intermediate resolution seismic reflection data combined with drill site information. The Antarctic Paleoenviron.: Perspect. Glob. Chang.: Part One 56, 231–264. https://doi.org/10.1029/ar056p0231.

Anderson, J.B., Conway, H., Bart, P.J., Witus, A.E., Greenwood, S.L., McKay, R.M., Hall, B.L., Ackert, R.P., Licht, K., Jakobsson, M., Stone, J.O., 2014. Ross Sea paleo-ice sheet drainage and deglacial history during and since the LGM. Quat. Sci. Rev. 100, 31–54. https://doi.org/10.1016/j.quascirev.2013.08.020.

Anderson, J.B., Simkins, L.M., Bart, P.J., De Santis, L., Halberstadt, A.R., Olivo, E., Greenwood, S.L., 2019. Seismic and geomorphic records of Antarctic Ice Sheet evolution in the Ross Sea and controlling factors in its behaviour. Geol. Soc. , London, Special Publ. 475, 223–240. https://doi.org/10.1144/SP475.5.

Arndt, J.E., Schenke, H.W., Jakobsson, M., Nitsche, F., Buys, G., Goleby, B., Rebesco, M., Bohoyo, F., Hong, J.K., Black, J., Greku, R., Udintsev, G., Barrios, F., Reynoso-Peralta, W., Morishita, T., Wigley, R., 2013. The international bathymetric chart of the Southern Ocean (IBCSO) version 1.0—a new bathymetric compilation covering circum-Antarctic waters. Geophys. Res. Lett. 40, 3111–3117. https://doi.org/10.1002/grl.50413.

Barker, P.F., Camerlenghi, A., 2002. Glacial history of the Antarctic Peninsula from Pacific margin sediments. Proc. Ocean Drill. Progr. Sci. Results 178, 1–40. https://doi.org/10.2973/odp.proc.sr.178.238.2002.

Barrett, P.J., 1989. Antarctic Cenozoic History from the CIROS-1 Drillhole, McMurdo Sound. DSIR Pub., p. 245

Barrett, P.J., Anderson, J.B., 2000. Grain size analysis of samples from CRP-2/2A, Victoria Land basin, Antarctica. Terra Antartica 7, 373–378.

Barrett, P.J., Sarti, M., Wise, S., 1998. Initial Report on CRP-3. Cape Roberts Project, Antarctica.

Bart, P.J., 2001. Did the Antarctic ice sheets expand in the early Pliocene? Geology 29 (1), 67–70. https://doi.org/10.1130/0091-7613(2001)029<0067:DTAISE>2.0.CO;2.

Bart, P.J., 2003. Were West Antarctic ice sheet grounding events in the Ross Sea a consequence of East Antarctic ice sheet expansion during the middle Miocene? Earth Planet Sci. Lett. 216, 93–107. https://doi.org/10.1016/s0012-821x(03)00509-0.

Bart, P.J., Cone, A.N., 2012. Early stall of West Antarctic Ice Sheet advance on the eastern Ross Sea middle shelf followed by retreat at 27,500 14C yr BP. Palaeogeogr. Palaeoclimatol. Palaeoecol. 335–336, 52–60.

Bart, P.J., De Santis, L., 2012. Glacial intensification during the Neogene: a review of seismic stratigraphic evidence from the Ross Sea, Antarctica, continental shelf. Oceanography 25, 166–183. https://doi.org/10.5670/oceanog.2012.92.

Bart, P.J., Anderson, J.B., Trincardi, F., Shipp, S.S., 2000. Seismic data from the Northern basin, Ross Sea, record extreme expansions of the East Antarctic ice sheet during the late Neogene. Mar. Geol. 166, 31–50. https://doi.org/10.1016/s0025-3227(00)00006-2.

Bart, P.J., Sjunneskog, C., Chow, J.M., 2011. Piston-core based biostratigraphic constraints on Pleistocene oscillations of the West Antarctic ice sheet in western Ross Sea between North Basin and AND-1B drill site. Mar. Geol. 289, 86–99. https://doi.org/10.1016/j.margeo.2011.09.005.

Behrendt, J.C., LeMasurier, W.E., Cooper, A.K., Tessensohn, F., Trehu, A., Damaske, D., 1991. Geophysical studies of the West Antarctic rift system. Tectonics 10, 1257–12733. https://doi.org/10.1029/91tc00868.

The RAISED Consortium, Bentley, M.J., Cofaigh, C.O., Anderson, J.B., Conway, H., Davies, B., Graham, A.G., 2014. A community-based geological reconstruction of Antarctic ice sheet deglaciation since the last glacial maximum. Quat. Sci. Rev. 100, 1–9.

Bergamasco, A., Defendi, V., Zambianchi, E., Spezie, G., 2002. Evidence of dense water overflow on the Ross Sea shelf-break. Antarct. Sci. 14, 271–277. https://doi.org/10.1017/s0954102002000068.

Blum, P., 1997. Physical properties handbook: a guide to the shipboard measurement of physical properties of deep-sea cores. ODP Tech. Note 26. https://doi.org/10.2973/odp.tn.26.1997.

Brancolini, G., Cooper, A.K., Barker, P.F., 1995a. Descriptive text for the seismic stratigraphic atlas of the Ross Sea. Geol. Sesmic.Strat. Antartic Margin 68, 271–303. https://doi.org/10.1002/9781118669013.app1.

Brancolini, G., Cooper, A.K., Coren, F., 1995b. Seismic facies and glacial history in the western Ross Sea (Antarctica). Geol. Seism. Strat. Antarctic Margin 68, 209–233. https://doi.org/10.1029/ar068p0209.

Budillon, G., Spezie, G., 2000. Thermohaline structure and variability in the terra Nova Bay polynya, Ross Sea. Antarct. Sci. 12, 493–508. https://doi.org/10.1017/s0954102000000572.

Budillon, G., Castagno, P., Aliani, S., Spezie, G., Padman, L., 2011. Thermohaline variability and Antarctic bottom water formation at the Ross Sea shelf break. Deep Sea Res. Oceanogr. Res. Pap. 58, 1002–1018. https://doi.org/10.1016/j.dsr.2011.07.002.

Callahan, J.E., 1972. The structure and circulation of deep water in the Antarctic. Deap Sea Res. Oceanogr. Abstr. 19, 563–575. https://doi.org/10.1016/0011-7471(72)90040-x.

Cande, S.C., Stock, J.M., Müller, R.D., Ishihara, T., 2000. Cenozoic motion between east and west Antarctica. Nature 404, 145–150. https://doi.org/10.1038/35004501.

Ceramicola, S., Rebesco, M., De Batist, M., Khlystov, O., 2001. Seismic evidence of small-scale lacustrine drifts in Lake Baikal (Russia). Mar. Geophys. Res. 22, 445–464. https://doi.org/10.1023/A:1016351700435.

Chavaillaz, Y., Codron, F., Kageyama, M., 2013. Southern westerlies in LGM and future (RCP4.5) climates. Clim. Past 9, 517–524. https://doi.org/10.5194/cp-9-517-2013.

Chen, P.-H., 1975. Antarctic radiolarians. In: Hayes, D.E., Frakes, L.A., et al. (Eds.), Initial Reports of the Deep Sea Drilling Project, 28: Washington, DC (U.S. GovernmentPrinting Office), pp. 437–513. https://doi.org/10.2973/dsdp.proc.28.111.1975.

Ciesielski, P.F., 1975. Biostratigraphy and paleoecology of Neogene and Oligocene silicoflagellates from cores recovered during Antarctic leg 28, Deep Sea Drilling Project. In: Hayes, Frakes, et al. (Eds.), Leg 28 DSDP Initial Report Volume, pp. 625–691. https://doi.org/10.2973/dsdp.proc.28.1975.

Colleoni, F., De Santis, L., Montoli, E., Olivo, E., Sorlien, C.C., Bart, P.J., Gasson, E.G.W., Bergamasco, A., Sauli, C., Wardell, N., Prato, S., 2018a. Past continental shelf evolution increased Antarctic ice sheet sensitivity to climatic conditions. Sci. Rep. 8, 1–12. https://doi.org/10.1038/s41598-018-29718-7.

Colleoni, F., De Santis, L., Siddoway, C.S., Bergamasco, A., Golledge, N.R., Lohmann, G., et al., 2018b. Spatio-temporal variability of processes across Antarctic ice-bed–ocean interfaces. Nat. Commun. 9 (1), 1–14.

Cook, C.P., Van De Flierdt, T., Williams, T., Hemming, S.R., Iwai, M., Kobayashi, M., Jimenez-Espejo, F.J., Escutia, C., González, J.J., Khim, B.K., McKay, R.M., Passchier, S., Bohaty, S.M., Riesselman, C.R., Tauxe, L., Sugisaki, S., Galindo, A.L., Patterson, M.O., Sangiorgi, F., Yamane, M., 2013. Dynamic behaviour of the East Antarctic ice sheet during Pliocene warmth. Nat. Geosci. 6, 765–769. https://doi.org/10.1038/ngeo1889.

Cooper, A.K., Davey, F.J., 1985. Episodic rifting of Phanerozoic rocks in the Victoria Land basin, western Ross Sea, Antarctica. Science 229, 1085–1087. https://doi.org/10.1126/science.229.4718.1085.

Cooper, A.K., Davey, F.J., Cochrane, G.R., 1987. Structure of extensionally rifted crust beneath the western Ross Sea and Iselin Bank, Antarctica, from sonobuoy seismic data. In: Cooper, A.K., Davey, F.J. (Eds.), The Antarctic Continental Margin: Geology and Geophysics of the Western Ross Sea, pp. 93–117.

Cooper, A.K., Barrett, P.J., Hinz, K., Traube, V., Letichenkov, G., Stagg, H.M., 1991. Cenozoic prograding sequences of the Antarctic continental margin: a record of glacio-eustatic and tectonic events. Mar. Geol. 102, 175–213. https://doi.org/10.1016/0025-3227(91)90008-r.

Cooper, A.K., Barker, P.F., Brancolini, G., Hambrey, M.J., 1995. Geology and Seismic Stratigraphy of the Antarctic Margin, vol. 68. https://doi.org/10.1029/ar068.

D'Agostino, A., Webb, P.N., 1980. Interpretation of mid-Miocene to recent lithostratigraphy and biostratigraphy at DSDP site 273, Ross Sea. Antarctic J. 15, 118–120.
Davey, F.J., Granot, R., Cande, S.C., Stock, J.M., Selvans, M., Ferraccioli, F., 2016. Synchronous oceanic spreading and continental rifting in West Antarctica. Geophys. Res. Lett. 43, 6162–6169. https://doi.org/10.1002/2016gl069087.
Davison, B.J., Cowton, T.R., Cottier, F.R., Sole, A.J., 2020. Iceberg melting substantially modifies oceanic heat flux towards a major Greenlandic tidewater glacier. Nat. Commun. 11 (1), 5983. https://doi.org/10.1038/s41467-020-19805-7.
De Santis, L., Anderson, J.B., Brancolini, G., Zayatz, I., 1995. Seismic record of late Oligocene through Miocene glaciation on the central and eastern continental shelf of the Ross Sea. Geol. Sesmic.Strat. Antartic Margin 68, 235–260. https://doi.org/10.1029/ar068p0235.
De Santis, L., Prato, S., Brancolini, G., Lovo, M., Torelli, L., 1999. The Eastern Ross Sea continental shelf during the Cenozoic: implications for the West Antarctic ice sheet development. Global Planet. Change 23, 173–196. https://doi.org/10.1016/s0921-8181(99)00056-9.
De Santis, L., Brancolini, G., Donda, F., 2003. Seismo-stratigraphic analysis of the Wilkes Land continental margin (East Antarctica): influence of glacially driven processes on the Cenozoic deposition. Deep Sea Res. Part II Top. Stud. Oceanogr. 50, 1563–1594. https://doi.org/10.1016/s0967-0645(03)00079-1.
Decesari, R.C., Sorlien, C.C., Luyendyk, B.P., Wilson, D.S., Bartek, L., Diebold, J., Hopkins, S.E., 2007. Regional seismic stratigraphic correlations of the Ross Sea: implications for the tectonic history of the West Antarctic rift system. In: Antarctica: A Keystone in a Changing World – Online Proceedings of the 10th ISAES, pp. 52–56. https://doi.org/10.3133/ofr20071047srp052.
DeConto, R.M., Pollard, D., 2016. Contribution of Antarctica to past and future sea-level rise. Nature 531, 591–597. https://doi.org/10.1038/nature17145.
Dinniman, M.S., Klinck, J.M., Smith Jr., W.O., 2003. Cross-shelf exchange in a model of the Ross Sea circulation and biogeochemistry. Deep Sea Res. Part II Top. Stud. Oceanogr. 50, 3103–3120. https://doi.org/10.1016/j.dsr2.2003.07.011.
Dinniman, M.S., Klinck, J.M., Smith Jr., W.O., 2011. A model study of Circumpolar deep Water on the West Antarctic Peninsula and Ross Sea continental shelves. Deep Sea Res. Part II Top. Stud. Oceanogr. 58, 1508–1523. https://doi.org/10.1016/j.dsr2.2010.11.013.
Diviacco, P., Rebesco, M., Camerlenghi, A., 2006. Late pliocene mega debris flow deposit and related fluid escapes identified on the antarctic peninsula continental margin by seismic reflection data analysis. Mar. Geophys. Res. 27, 1–19. https://doi.org/10.1007/s11001-005-3136-8.
Donda, F., Brancolini, G., O'Brien, P.E., De Santis, L., Escutia, C., 2007. Sedimentary processes in the Wilkes Land margin: a record of the Cenozoic East Antarctic ice sheet evolution. J. Geol. Soc. 164, 243–256. https://doi.org/10.1144/0016-7649er164-1.
Donda, F., O'Brien, P.E., De Santis, L., Rebesco, M., Brancolini, G., 2008. Mass wasting processes in the Western Wilkes Land margin: possible implications for East Antarctic glacial history. Palaeogeogr. Palaeoclimatol. Palaeoecol. 260, 77–91. https://doi.org/10.1016/j.palaeo.2007.08.008.
Donda, F., Leitchenkov, G., Brancolini, G., Romeo, R., De Santis, L., Escutia, C., O'Brien, P., Armand, L., Caburlotto, A., Cotterle, D., 2020. The influence of totten glacier on the late Cenozoic sedimentary record. Antarct. Sci. 32, 288–300. https://doi.org/10.1017/s0954102020000188.
Dowdeswell, J.A., Cofaigh, C.Ó., Pudsey, C.J., 2004. Continental slope morphology and sedimentary processes at the mouth of an Antarctic palaeo-ice stream. Mar. Geol. 204, 203–214. https://doi.org/10.1016/s0025-3227(03)00338-4.
Eagles, G., Gohl, K., Larter, R.D., 2004. High-resolution animated tectonic reconstruction of the south Pacific and West Antarctic margin. G-cubed 5. https://doi.org/10.1029/2003gc000657.
Escutia, C., Nelson, C.H., Acton, G.D., Eittreim, S.L., Cooper, A.K., Warnke, D.A., Jaramillo, J.M., 2002. Current Controlled Deposition on the Wilkes Land Continental Rise, Antarctica, vol. 22. Geological Society, London, Memoirs, pp. 373–384. https://doi.org/10.1144/gsl.mem.2002.022.01.26.
Escutia, C., Bárcena, M.A., Lucchi, R.G., Romero, O., Ballegeer, A.M., Gonzalez, J.J., Harwood, D.M., 2009. Circum-Antarctic warming events between 4 and 3.5 Ma recorded in marine sediments from the Prydz Bay (ODP Leg 188) and the antarctic Peninsula (ODP Leg 178) margins. Global Planet. Change 69, 170–184. https://doi.org/10.1016/j.gloplacha.2009.09.003.
Faugères, J.-C., Stow, D.A.V., Imbert, P., Viana, A.R., 1999. Seismic features diagnostic of contourite drifts. Mar. Geol. 162, 1–38.
Flower, B.P., Kennett, J.P., 1993. Middle Miocene ocean-climate transition: high-resolution oxygen and carbon isotopic records from Deep Sea Drilling Project Site 588A, southwest Pacific. Paleoceanography 8, 811–843. https://doi.org/10.1029/93pa02196.
Fretwell, P., Pritchard, H.D., Vaughan, D.G., Bamber, J.L., Barrand, N.E., Bell, R., Bianchi, C., Bingham, R.G., Blankenship, D.D., Casassa, G., Catania, G., Callens, D., Conway, H., Cook, A.J., Corr, H.F.J., Damaske, D., Damm, V., Ferraccioli, F., Forsberg, R., et al., 2012. Bedmap2: improved ice bed, surface and thickness datasets for Antarctica. TCD 6, 4305–4361. https://doi.org/10.5194/tc-7-375-2013.
Gales, J., Rebesco, M., De Santis, L., Bergamasco, A., Colleoni, F., Kim, S., Accettella, D., Kovacevic, V., Liu, Y., Olivo, E., Colizza, E., Florindo-Lopez, C., Zgur, F., McKay, R., 2021. Role of dense shelf water in the development of Antarctic submarine canyon morphology. Geomorphology 372, 107453.
Giorgetti, A., Crise, A., Laterza, R., Perini, L., Rebesco, M., Camerlenghi, A., 2003. Water masses and bottom boundary layer dynamics above a sediment drift of the Antarctic Peninsula Pacific margin. Antarct. Sci. 15, 537–546. https://doi.org/10.1017/s0954102003001652.
Golledge, N.R., Fogwill, C.J., Mackintosh, A.N., Buckley, K.M., 2012. Dynamics of the last glacial maximum Antarctic ice-sheet and its response to ocean forcing. Proc. Natl. Acad. Sci. Unit. States Am. 109, 16052–16056. https://doi.org/10.1073/pnas.1205385109.
Gordon, A.L., 2009. Bottom water formation. In: Steele, J.H., Thorpe, S.A., Turekian, K. (Eds.), Ocean Currents, pp. 263–269. https://doi.org/10.1006/rwos.2001.0006.
Gouretski, V., 1999. The large-scale thermohaline structure of the Ross Gyre. In: Manzella, G.M., Spezie, G. (Eds.), Oceanography of the Ross Sea, pp. 77–100. https://doi.org/10.1007/978-88-470-2250-8_6. Antarctica.
Granot, R., Dyment, J., 2018. Late Cenozoic unification of East and West Antarctica. Nat. Commun. 9, 1–10. https://doi.org/10.1038/s41467-018-05270-w.
Grützner, J., Rebesco, M., Cooper, A.K., Forsberg, C.F., Kryc, K.A., Wefer, G., 2003. Evidence for orbitally controlled size variations of the East Antarctic ice sheet during the late Miocene. Geology 31, 777–780. https://doi.org/10.1130/g19574.1.
Halberstadt, A.R., Simkins, L.M., Greenwood, S.L., Anderson, J.B., 2016. Past ice-sheet behaviour: retreat scenarios and changing controls in the Ross Sea, Antarctica. Cryosphere 10, 1003–1020. https://doi.org/10.5194/tc-10-1003-2016.
Haq, B.U., Hardenbol, J.A., Vail, P.R., 1987. Chronology of fluctuating sea levels since the Triassic. Science 235, 1156–1167. https://doi.org/10.1126/science.235.4793.1156.
Hayes, D.E., Frakes, L.A., 1975. Initial Reports of the Deep Sea Drilling Project, vol. 28.
Herbert, T.D., Lawrence, K.T., Tzanova, A., Peterson, L.C., Caballero-Gill, R., Kelly, C.S., 2016. Late Miocene global cooling and the rise of modern ecosystems. Nat. Geosci. 9, 843–847. https://doi.org/10.1038/ngeo2813.
Hernàndez-Molina, F.J., Llave, E., Somoza, L., Fernàndez-Puga, M.C., Maestro, A., Leòn, R., Medialdea, T., Barnolas, A., García, M., Díaz del Río, V., Fernández-Salas, L. M., Tomás Vázquez, J., Lobo, F., Alveirinho Dias, J.M., Rodero, J., Gardner, J., 2003. Looking for clues to paleoceanographic imprints: a diagnosis of the Gulf of Cadiz contourite depositional systems. Geology 31, 19–22. https://doi.org/10.1130/0091-7613(2003)031%3C0019:lfctpi%3E2.0.co;2.
Hernández-Molina, F.J., Maldonado, A., Stow, D.A., 2008. Abyssal plain contourites. Dev. Sedimentol. 60, 345–378. https://doi.org/10.1016/s0070-4571(08)10018-8.
Hernández-Molina, F.J., Paterlini, M., Violante, R., Marshall, P., De Isasi, M., Somoza, L., Rebesco, M., 2009. Contourite depositional system on the Argentine Slope: an exceptional record of the influence of Antarctic water masses. Geology 37, 507–510. https://doi.org/10.1130/g25578a.1.
Hernández-Molina, F.J., Stow, D.A., Llave, E., Rebesco, M., Ercilla, G., van Rooij, D., Mena, A., Vazquez, J.T., Voelker, A.H., 2011. Deep-water circulation: processes products (16–18 June 2010, Baiona): introduction and future challenges. Geo Mar. Lett. 31, 285–300. https://doi.org/10.1007/s00367-011-0261-z.
Hernández-Molina, F.J., Wåhlin, A., Bruno, M., Ercilla, G., Llave, E., Serra, N., Rosón, G., Puig, P., Rebesco, M., Van Rooij, D., Roque, D., González-Pola, C., Sánchez, F., Gómez, M., Preu, B., Schwenk, T., Hanebuth, T.J.J., Sánchez Leal, R.F., García-Lafuente, J., Brackenridge, R.E., Juan, C., Stow, D.A.V., Sánchez-González, J.M., 2016. Oceanographic processes and morphosedimentary products along the Iberian margins: a new multidisciplinary approach. Mar. Geol. 378, 127–156. https://doi.org/10.1016/j.margeo.2015.12.008.
Hernández-Molina, F.J., Larter, R.D., Maldonado, A., 2017. Neogene to quaternary stratigraphic Evolution of the Antarctic Peninsula, Pacific margin offshore of Adelaide Island: transitions from a non-glacial, through glacially-influenced to a fully glacial state. Global Planet. Change 156, 80–111. https://doi.org/10.1016/j.gloplacha.2017.07.002.
Hillenbrand, C.D., Cortese, G., 2006. Polar stratification: a critical view from the Southern Ocean. Palaeogeogr. Palaeoclimatol. Palaeoecol. 242, 240–252. https://doi.org/10.1016/j.palaeo.2006.06.001.
Hinz, K., Block, M., 1984. Results of geophysical in-vestigations in the Weddell Sea and in the Ross Sea, Antarctica. in Proceedings of the 11th World Petro-leum Congress: Chichester, London, UK, John Wiley & Sons, Geology Exploration Reserves 2, 79–91.
Huang, X., Stärz, M., Gohl, K., Knorr, G., Lohmann, G., 2017. Impact of Weddell Sea shelf progradation on Antarctic bottom water formation during the Miocene. Paleoceanography 32 (3), 304–317.
Jacobs, S.S., 1991. On the nature and significance of the Antarctic Slope Front. Mar. Chem. 35, 9–24. https://doi.org/10.1016/s0304-4203(09)90005-6.
Jacobs, S.S., Giulivi, C.F., 1999. Thermohaline data and ocean circulation on the Ross Sea continental shelf. In: Spezie, G., Manzella, G.M. (Eds.), Oceanography of the Ross Sea, pp. 3–16. https://doi.org/10.1007/978-88-470-2250-8_1. Antarctica.
Jacobs, S.S., Amos, A.F., Bruchhausen, P.M., 1970. Ross Sea oceanography and Antarctic bottom Water formation. Deap Sea Res. Oceanogr. Abstr. 17, 935–962. https://doi.org/10.1016/0011-7471(70)90046-x.
Jacobs, S.S., Fairbanks, R.G., Horibe, Y., 1985. Origin and evolution of water masses near the Antarctic continental margin: evidence from H2 18O/H2 16O ratios in seawater. In: Jacobs, S.S. (Ed.), Oceanology of the Antarctic Continental Shelf, vol. 43, pp. 59–85. https://doi.org/10.1029/ar043p0059.
Jacobs, S.S., Helmer, H.H., Doake, C.S., Jenkins, A., Frolich, R.M., 1992. Melting of ice shelves and the mass balance of Antarctica. J. Glaciol. 38, 375–387. https://doi.org/10.3189/s0022143000002252.
Joughin, I., Alley, R.B., 2011. Stability of the West Antarctic ice sheet in a warming world. Nat. Geosci. 4 (8), 506–513.
Kim, S., De Santis, L., Hong, J.K., Cottlerle, D., Petronio, L., Colizza, E., Kim, Y.G., Kang, S.G., Kim, H.J., Kim, S., Wardell, N., Geletti, R., Bergamasco, A., McKay, R., Jin, Y.K., Kang, S., 2018. Seismic stratigraphy of the Central Basin in northwestern Ross Sea slope and rise, Antarctica: clues to the late Cenozoic ice-sheet dynamics and bottom-current activity. Mar. Geol. 395, 363–379. https://doi.org/10.1016/j.margeo.2017.10.013.

Kohfeld, K.E., Graham, R.M., De Boer, A.M., Sime, L.C., Wolff, E.W., Le Quéré, C., Bopp, L., 2013. Southern Hemisphere westerly wind changes during the Last Glacial Maximum: paleo-data synthesis. Quat. Sci. Rev. 68, 76–95.

Kohut, J., Hunter, E., Huber, B., 2013. Small-scale variability of the cross-shelf flow over the outer shelf of the Ross Sea. J. Geophys. Res.: Oceans 118, 1863–1876. https://doi.org/10.1002/jgrc.20090.

Kulhanek, D.K., Levy, R.H., Clowes, C.D., Prebble, J.G., Rodelli, D., Jovane, L., Morgans, H.E.G., Kraus, C., Zwingmann, H., Griffith, E.M., Scher, H.D., McKay, R.M., Naish, T.R., 2019. Revised chronostratigraphy of DSDP site 270 and late Oligocene to early Miocene paleoecology of the Ross Sea sector of Antarctica. Global Planet. Change 178, 46–64. https://doi.org/10.1016/j.gloplacha.2019.04.002.

Kuvaas, B., Leitchenkov, G., 1992. Glaciomarine turbidite and current controlled deposits in Prydz Bay, Antarctica. Mar. Geol. 108, 365–381. https://doi.org/10.1016/0025-3227(92)90205-v.

Laberg, J.S., Camerlenghi, A., 2008. The significance of contourites for submarine slope stability. Dev. Sedimentol. 60, 537–556. https://doi.org/10.1016/s0070-4571(08)10025-5.

Lamy, F., Kilian, R., Arz, H.W., Francois, J.P., Kaiser, J., Prange, M., Steinke, T., 2010. Holocene changes in the position and intensity of the southern westerly wind belt. Nat. Geosci. 3 (10), 695–699.

Leckie, M., Webb, P.N., 1986. Late Paleogene and early Neogene foraminifers of deep sea drilling Project site 270, Ross Sea. Initial Rep. DSDP 90, 1093–1142. https://doi.org/10.2973/dsdp.proc.90.124.1986.

Lee, C., Nott, J.A., Keller, F.B., 2004. Seismic expression of the Cenozoic mass transport complexes, deepwater Tarfaya-Agadir basin, offshore Morocco. In: Offshore Technology Conference Proceedings. https://doi.org/10.4043/16741-ms.

LeMasurier, W.E., 1990. Late Cenozoic volcanism on the Antarctic plate: an overview. Volc. Antarctic Plate South. Oceans 48, 1–17. https://doi.org/10.1029/ar048p0001.

Levy, R.H., Meyers, S.R., Naish, T.R., Golledge, N.R., McKay, R.M., Crampton, J.S., DeConto, R.M., De Santis, L., Florindo, F., Gasson, E.G.W., Harwood, D.M., Luyendyk, B.P., Powell, R.D., Clowes, C., Kulhanek, D.K., 2019. Antarctic ice-sheet sensitivity to obliquity forcing enhanced through ocean connections. Nat. Geosci. 12, 132–137. https://doi.org/10.1038/s41561-018-0284-4.

Lindeque, A., Gohl, K., Henrys, S., Wobbe, F., Davy, B., 2016. Seismic stratigraphy along the Amundsen Sea to Ross Sea continental rise: a cross-regional record of pre-glacial to glacial processes of the West Antarctic margin. Palaeogeogr. Palaeoclimatol. Palaeoecol. 443, 183–202. https://doi.org/10.1016/j.palaeo.2015.11.017.

Lucchi, R.G., Rebesco, M., 2007. Glacial contourites on the Antarctic Peninsula margins: insight for palaeoenvironmental and palaeoclimatic conditions. In: Viana, A.R., Rebesco, M. (Eds.), Economic and Palaeosignificance of Contourite Deposits, vol. 276. Geological Society of London special publication, pp. 111–127.

Lucchi, R.G., Rebesco, M., Camerlenghi, A., Busetti, M., Tomadin, L., Villa, G., Persico, D., Morigi, C., Bonci, M.C., Giorgetti, G., 2002. Glacimarine sedimentary Processes of a high-latitude, deep-sea sediment drift (Antarctic Peninsula Pacific margin). Mar. Geol. 189, 343–370.

Lucchi, R.G., Caburlotto, A., Miserocchi, S., Liu, Y., Morigi, C., Persico, D., Villa, G., Langone, L., Colizza, E., Macrì, P., Sagnotti, L., Conte, R., Rebesco, M., 2019. The depositional record of the Odyssea drift (Ross Sea, Antarctica). In: European Geosciences Union (EGU) General Assembly 2019, Vienna April, 7th-12th, Geophysical Research Abstracts, 21. EGU2019-10409-1, 2019.

Luyendyk, B.P., Sorlien, C.C., Wilson, D.S., Bartek, L.R., Siddoway, C.S., 2001. Structural and tectonic evolution of the Ross Sea rift in the Cape Colbeck region, Eastern Ross Sea, Antarctica. Tectonics 20, 933–958. https://doi.org/10.1029/2000tc001260.

Mack, S.L., Dinniman, M.S., McGillicuddy, D.J., Sedwick, P.N., Klinck, J.M., 2017. Dissolved iron transport pathways in the Ross Sea: influence of tides and horizontal resolution in a regional ocean model. J. Mar. Syst. 166, 73–86. https://doi.org/10.1016/j.jmarsys.2016.10.008.

Maldonado, A., Barnolas, A., Bohoyo, F., Escutia, C., Galindo-Zaldívar, J., Hernández-Molina, J., Jabaloy, A., Lobo, F.J., Nelson, C.H., Rodríguez-Fernández, J., Somoza, L., Vázquez, J.-T., 2005. Miocene to Recent contourite drifts development in the northern Weddell Sea (Antarctica). Global Planet. Change 45, 99–129. https://doi.org/10.1016/j.gloplacha.2004.09.013.

McDougall, I., 1977. Potassium-argon dating of glauconite from a greensand drilled at site 270 in the Ross Sea, DSDP Leg 28. In: Initial Reports of the Deep Sea Drilling Project, pp. 1071–1072. https://doi.org/10.2973/dsdp.proc.36.281.1977.

McKay, R., Naish, T., Carter, L., Riesselman, C., Dunbar, R., Sjunneskog, C., Winter, D., Sangiorgi, F., Warren, C., Pagani, M., Schouten, S., Willmott, V., Levy, R., DeConto, R., Powell, R.D., 2012. Antarctic and Southern Ocean influences on late Pliocene global cooling. Proc. Natl. Acad. Sci. Unit. States Am. 109, 6423–6428. https://doi.org/10.1073/pnas.1112248109.

McKay, R.M., Barrett, P.J., Levy, R.S., Naish, T.R., Golledge, N.R., Pyne, A., 2016. Antarctic Cenozoic climate history from sedimentary records: ANDRILL and beyond. Phil. Trans. Math. Phys. Eng. Sci. 374, 20140301. https://doi.org/10.1098/rsta.2014.0301.

McKay, R., De Santis, L., Kulhanek, D., Exp. 374 Scientists, 2019. Ross Sea West Antarctic ice sheet history. Proc. Int. Ocean Disc. Prog. Exped. 374 https://doi.org/10.14379/iodp.proc.374.2019.

Michels, K., Rogenhagen, J., Kuhn, G., 2001. Recognition of contour-current influence in mixed contourite-turbidite sequences of the western Weddell Sea, Antarctica. Mar. Geophys. Res. 22, 465–485. https://doi.org/10.1144/gsl.mem.2002.022.01.22.

Miller, K.G., Wright, J.D., Browning, J.V., Kulpecz, A., Kominz, M., Naish, T.R., Cramer, B.S., Rosenthal, Y., Peltier, W.R., Sosdian, S., 2012. High tide of the warm Pliocene: implications of global sea level for Antarctic deglaciation. Geology 40 (5), 407–410. https://doi.org/10.1130/G32869.1.

Morrison, A.K., Hogg, A.M., England, M.H., Spence, P., 2020. Warm Circumpolar Deep Water transport toward Antarctica driven by local dense water export in canyons. Sci. Adv. 6 https://doi.org/10.1126/sciadv.aav2516 eaav2516.

Moscardelli, L., Wood, L., 2008. New classification system for mass transport complexes in offshore Trinidad. Basin Res. 20, 73–98. https://doi.org/10.1111/j.1365-2117.2007.00340.x.

Naish, T., Powell, R., Levy, R., Wilson, G., Scherer, R., Talarico, F., Krissek, L., Niessen, F., Pompilio, M., Wilson, T., Carter, L., DeConto, R., Huybers, P., McKay, R., Pollard, D., Ross, J., Winter, D., Barrett, P., Browne, G., Williams, T., 2009. Obliquity-paced Pliocene West Antarctic ice sheet oscillations. Nature 458, 322–328. https://doi.org/10.1038/nature07867.

Orsi, A.H., Wiederwohl, C.L., 2009. A recount of Ross Sea waters. Deep Sea Res. Part II Top. Stud. Oceanogr. 56, 778–795. https://doi.org/10.1016/j.dsr2.2008.10.033.

Orsi, A.H., Johnson, G.C., Bullister, J.L., 1999. Circulation, mixing, and production of Antarctic bottom Water. Prog. Oceanogr. 43, 55–109. https://doi.org/10.1016/s0079-6611(99)00004-x.

Patterson, M.O., McKay, R., Naish, T., Escutia, C., Jimenez-Espejo, F.J., Raymo, M.E., Meyers, S.M., Tauxe, L., Brinkhuis, H., 2014. Orbital forcing of the East Antarctic ice sheet during the Pliocene and Early Pleistocene. Nat. Geosci. 7, 841–847. https://doi.org/10.1038/ngeo2273.

Pérez, L.F., De Santis, L., McKay, R.M., Larter, R.D., Ash, J., Bart, P.J., Böhm, G., Brancatelli, G., Browne, I., Colleoni, F., Dodd, J.P., Geletti, R., Harwood, D.M., Kuhn, G., Laberg, J.S., Leckie, R.M., Levy, R.H., Marschalek, J., Mateo, Z., Naish, T. R., Sangiorgi, F., Shevenell, A.E., Sorlien, C.C., van de Flierdt, T., International Ocean Discovery Program Expedition 374 Scientists, 2021a. Early and middle Miocene ice sheet dynamics in the Ross Sea: results from integrated core-log-seismic interpretation. GSA Bull. https://doi.org/10.1130/B35814.1.

Pérez, L.F., Martos, Y.M., García, M., Weber, M.E., Raymo, M.E., Williams, T., Bohoyo, F., Armbrecht, L., Bailey, I., Brachfeld, S., Glüder, A., Guitard, M., Gutjahr, M., Hemming, S., Hernández-Almeida, I., Hoem, F.S., Kato, Y., O'Connell, S., Peck, V.L., Reilly, B., Ronge, T.A., Tauxe, L., Warnock, J., Zheng, X., the IODP Expedition 382 Scientists, 2021b. Miocene to present oceanographic variability in the Scotia Sea and Antarctic ice sheets dynamics: insight from revised seismic-stratigraphy following IODP Expedition 382. Earth Planet Sci. Lett. 553, 116657.

Piper, D.J., Brisco, C.D., 1975. Deep-water continental-margin sedimentation. Initial Rep. Deep Sea Drill. Proj. 28, 727–755. https://doi.org/10.2973/dsdp.proc.28.121.1975.

Posamentier, H.W., Kolla, V., 2003. Seismic geomorphology and stratigraphy of depositional elements in deep-water settings. J. Sediment. Res. 73, 367–388. https://doi.org/10.1306/111302730367.

Prothro, L.O., Simkins, L.M., Majewski, W., Anderson, J.B., 2018. Glacial retreat patterns and processes determined from integrated sedimentology and geomorphology records. Mar. Geol. 395, 104–119. https://doi.org/10.1016/j.margeo.2017.09.012.

Prothro, L.O., Majewski, W., Yokoyama, Y., Simkins, L.M., Anderson, J.B., Yamane, M., Miyairi, Y., Ohkouchi, N., 2020. Timing and pathways of East Antarctic ice sheet retreat. Quat. Sci. Rev. 230, 106166. https://doi.org/10.1016/j.quascirev.2020.106166.

Rebesco, M., Camerlenghi, A., 2008. Late Pliocene margin development and mega debris flow deposits on the Antarctic continental margins: Evidence of the onset of the modern Antarctic Ice Sheet? Palaeogeogr. Palaeoclimatol. Palaeoecol. 260, 149–167. https://doi.org/10.1016/j.palaeo.2007.08.009.

Rebesco, M., Stow, D., 2001. Seismic expression of contourites and related deposits: a preface. Mar. Geophys. Res. 22, 303–308. https://doi.org/10.1023/A:1016316913639.

Rebesco, M., Camerlenghi, A., Zanolla, C., 1998. Bathymetry and morphogenesis of the continental margin west of the Antarctic Peninsula. Terra Antarctica 5, 715–725.

Rebesco, M., Pudsey, C., Canals, M., Camerlenghi, A., Barker, P., Estrada, F., Giorgetti, A., 2002. Sediment drifts and deep-sea channel systems, Antarctic Peninsula Pacific margin. Geol. Soc. London, Memoirs 22, 353–371. https://doi.org/10.1144/gsl.mem.2002.022.01.25.

Rebesco, M., Camerlenghi, A., Volpi, V., Neagu, C., Accettella, D., Lindberg, B., Cova, A., Zgur, F., 2007. Interaction of processes and importance of contourites: insights from the detailed morphology of sediment Drift 7, Antarctica. Geol. Soc. Spec. Publ. 276, 95–110. https://doi.org/10.1144/gsl.sp.2007.276.01.05.

Rebesco, M., Hernández-Molina, F.J., Van Rooij, D., Wåhlin, A., 2014. Contourites and associated sediments controlled by deep-water circulation processes: state-of-the-art and future considerations. Mar. Geol. 352, 111–154. https://doi.org/10.1016/j.margeo.2014.03.011.

Ryan, W.B.F., Carbotte, S.M., Coplan, J.O., O'Hara, S., Melkonian, A., Arko, R., Weissel, R.A., Ferrini, V., Goodwillie, A., Nitsche, F., Bonczkowski, J., Zemsky, R., 2009. Global multi-resolution Topography synthesis. Geochem. Geophys. Geosyst 10. https://doi.org/10.1029/2008gc002332.

Salvini, F., Brancolini, G., Busetti, M., Storti, F., Mazzarini, F., Coren, F., 1997. Cenozoic geodynamics of the Ross Sea region, Antarctica: crustal extension, intraplate strike-slip faulting, and tectonic inheritance. J. Geophys. Res.: Solid Earth 102, 24669–24696. https://doi.org/10.1029/97jb01643.

Sauermilch, I., Mateo, Z.R.P., Boaga, J., 2019. A comparative analysis of time–depth relationships derived from scientific ocean drilling expeditions. Mar. Geophys. Res. 40, 635–641. https://doi.org/10.1007/s11001-019-09393-7.

Savage, M.L., Ciesielski, P.F., 1983. A revised history of glacial sedimentation in the Ross Sea region. Antarctic Earth Sci. Int. Symp. 4, 555–559.

Scheuer, C., Gohl, K., Larter, R., Rebesco, M., Udintsev, G., 2006. Variability in Cenozoic sedimentation along the continental rise of the Bellingshausen sea, West Antarctica. Mar. Geol. 227, 279–298. https://doi.org/10.1016/j.margeo.2005.12.007.

Schmidtko, S., Heywood, K.J., Thompson, A.F., Aoki, S., 2014. Multidecadal warming of Antarctic waters. Science 346, 1227–1231. https://doi.org/10.1126/science.1256117.

Schoof, C., 2007. Ice sheet grounding line dynamics: steady states, stability, and hysteresis. J. Geophys. Res.: Earth Surface 112. https://doi.org/10.1029/2006JF000664.

Ship, S., Anderson, J., Domack, E., 1999. Late Pleistocene-holocene retreat of the West Antarctic ice-sheet system in the Ross Sea: part 1-geophysical results. Geol. Soc. Am. Bull. *111*, 1486–1516. https://doi.org/10.1130/0016-7606(1999)111%3C1486:LPHROT%3E2.3.CO;2.

Solli, K., Kuvaas, B., Kristoffersen, Y., Leitchenkov, G., Guseva, J., Gandjukhin, V., 2007. Seismic morphology and distribution of inferred glaciomarine deposits along the East Antarctic continental margin, 20°E-60°E. Mar. Geol. 237, 207–223. https://doi.org/10.1016/j.margeo.2006.12.002.

Somoza, L., Medialdea, T., González, F.J., 2019. Giant mass-transport deposits in the southern Scotia Sea (Antarctica). Geol. Soc. , London, Special Publ. 477 (1), 195–205.

Spence, P., Griffies, S.M., England, M.H., Hogg, A.M., Saenko, O.A., Jourdain, N.C., 2014. Rapid subsurface warming and circulation changes of Antarctic coastal waters by poleward shifting winds. Geophys. Res. Lett. 41, 4601–4610. https://doi.org/10.1002/2014gl060613.

Steinhauff, D.M., Webb, P.N., 1987. Miocene foraminifera from DSDP site 270, Ross Sea. Antarct. J. U. S. 22, 125–126.

Stow, D.A., Faugères, J.C., Howe, J.A., Pudsey, C.J., Viana, A.R., 2002. Bottom currents, contourites and deep-sea sediment drifts: current state-of-the-art. Geol. Soc. London, Memoirs 22, 7–20. https://doi.org/10.1144/gsl.mem.2002.022.01.02.

Sverdrup, H., 1940. Hydrology, section 2, discussion. *Reports of the B.A.N.Z.* In: Antarctic Research Expedition 1921–*1931*, 3, pp. 88–126.

Taviani, M., Reid, D.E., Anderson, J.B., 1993. Skeletal and isotopic composition and paleoclimatic significance of late Pleistocene carbonates, Ross Sea, Antarctica. J. Sediment. Res. 63, 84–90. https://doi.org/10.1306/d4267a96-2b26-11d7-8648000102c1865d.

Taylor-Silva, B.I., Riesselman, C.R., 2018. Polar frontal migration in the warm late Pliocene: diatom evidence from the Wilkes Land margin, East Antarctica. Paleoceanogr. Paleoclimatol. 33, 76–92. https://doi.org/10.1002/2017pa003225.

Thomas, R.H., Bentley, C.R., 1978. A model for Holocene retreat of the West Antarctic ice sheet. Quat. Res. 10, 150–170. https://doi.org/10.1016/0033-5894(78)90098-4.

Thompson, A., Stewart, A., Spence, P., Heywood, K., 2018. The Antarctic slope current in a changing climate. Rev. Geophys. 56, 741–770. https://doi.org/10.1029/2018rg000624.

Tinto, K.J., Padman, L., Siddoway, C.S., Springer, S.R., Fricker, H.A., Das, I., Caratori Tontini, F., Porter, D.F., Frearson, N.P., Howard, S.L., Siegfried, M.R., Mosbeux, C., Becker, M.K., Bertinato, C., Boghosian, A., Brady, N., Burton, B.L., Chu, W., Cordero, S.I., et al., 2019. Ross Ice Shelf response to climate driven by the tectonic imprint on seafloor bathymetry. Nat. Geosci. 12, 441–449. https://doi.org/10.1038/s41561-019-0370-2.

Uenzelmann-Neben, G., Gohl, K., 2014. Early glaciation already during the Early Miocene in the Amundsen sea, southern Pacific: indications from the distribution of sedimentary sequences. Global Planet. Change 120, 92–104. https://doi.org/10.1016/j.gloplacha.2014.06.004.

Volpi, V., Camerlenghi, A., Moerz, T., Corubolo, P., Rebesco, M., Tinivella, U., 2001. Data report: Physical Properties relevant to seismic stratigraphic studies, continental rise sites 1095, 1096, and 1101, ODP Leg 178, Antarctic Peninsula. Proc. Ocean Drill. Progr. 178 https://doi.org/10.2973/odp.proc.sr.178.228.2001.

Wåhlin, A.K., Steiger, N., Darelius, E., Assmann, K.M., Glessmer, M.S., Ha, H.K., et al., 2020. Ice front blocking of ocean heat transport to an Antarctic ice shelf. Nature 578 (7796), 568–571. https://doi.org/10.1038/s41586-020-2014-5.

Walker, D.P., Brandon, M.A., Jenkins, A., Allen, J.T., Dowdeswell, J.A., Evans, J., 2007. Oceanic heat transport onto the Amundsen Sea shelf through a submarine glacial trough. Geophys. Res. Lett. 34 https://doi.org/10.1029/2006gl028154.

Whitehead, J.M., Wotherspoon, S., Bohaty, S.M., 2005. Minimal Antarctic sea ice during the Pliocene. Geology 33, 137–140. https://doi.org/10.1130/g21013.1.

Whitworth, T., Orsi, A.H., Kim, S.J., Nowlin Jr., W.D., Locarnini, R.A., 1998. Water masses and mixing near the Antarctic slope front. In: Jacobs, S.S., Weiss, R.F. (Eds.), Ocean, Ice, and Atmosphere: Interactions at the Antarctic Continental Margin, pp. 1–27. https://doi.org/10.1029/ar075p0001.

Wilson, D.S., Luyendyk, B.P., 2009. West Antarctic paleotopography estimated at the Eocene-Oligocene climate transition. Geophys. Res. Lett. 36 https://doi.org/10.1029/2009gl039297.

Zhang, Z.S., et al., 2013. Mid-Pliocene Atlantic meridional overturning circulation not unlike modern? Clim. Past 9, 1495–1504.